Multicellular states of viscoelastic thermovibrational convection in a square cavity (EP)

View Online   Export Citation   CrossMark

Alessio Boaro [iD] and Marcello Lappa[a] [iD]

AFFILIATIONS

Department of Mechanical and Aerospace Engineering, University of Strathclyde, James Weir Building, 75 Montrose Street,
Glasgow G1 1XJ, United Kingdom

[a] Author to whom correspondence should be addressed: marcello.lappa@strath.ac.uk

ABSTRACT

The problem of pure *thermovibrational* flow in a two-dimensional square cavity containing a viscoelastic liquid is investigated in the framework of a numerical approach based on the governing balance equations for mass, momentum, and energy in their complete and non-linear time-dependent form. For problem closure, these equations are complemented with the transport equation for the elastic stress formulated using the finitely extensible nonlinear elastic Chilcott–Rallison (FENE–CR) constitutive model. A complete parametric study is carried out to highlight the different path of evolution taken by the considered viscoelastic fluid with respect to the corresponding Newtonian counterpart when the Gershuni number is increased. Attention is paid to the patterning scenario in terms of time-averaged flow and related multicellular structures. It is shown that the triadic relationship among the typical characteristic time scales involved in these phenomena, namely, the thermally diffusive time, the fluid relaxation time, and the period of vibrations, can lead to a kaleidoscope of states, which differ in regard to the prevailing symmetry and the related spatiotemporal behaviors. Moreover, the complex interaction between the external vibrations and the elastic property of the polymer molecules, mediated by viscous effects, can produce an interesting "intermittent response."

I. INTRODUCTION

Apart from the purely theoretical interest that attaches to the mathematical representation of viscoelastic fluids and their non-linear dynamics, these liquids find a wide spectrum of versatile applications in many fields of science and engineering. Relevant examples range from the development of plastic materials to a variety of complex fluids, which include (but are not limited to) colloids, polymer solutions, and particulate suspensions with often counter-intuitive fluid mechanical behavior.

For these reasons, over the years, viscoelastic fluids have been the subject of interest both in academia and industry. By definition, this class of fluids can exhibit a viscous and an elastic response at the same time. Therefore, they are able to retain stresses even if no velocity gradient is effective in the entire considered physical domain. As a natural consequence, a variety of interesting phenomena can be produced due to the intrinsically non-linear behavior, such as *rod-climbing*,[1] *extrude swell* or "*die swell*" effect (Ref. 2 and references therein), *the tubeless siphon*,[3] *the Uebler* effect,[4] *elastic recoil*,[5] and *vortex inhibition*[6] just to mention some of them.

More recently, significant interest has been attracted by flows of "natural" origin, i.e., convection produced by buoyancy (thermogravitational flow) or surface-tension effects (thermocapillary or "Marangoni" flow). Relevant examples pertaining to these lines of inquiry are indeed, Refs. 7–18 and 19–21, for buoyancy and Marangoni convection, respectively.

As revealed by these studies, whereas thermal convection in Newtonian fluids can be organized in well-defined universality classes, the interpretation of viscoelastic flow realizations is always more challenging, due to the inherent complexity and unpredictability.

In particular, this work examines the consequence of a long-held weakness of the existing literature, a problem which appears to have never been considered before, i.e., the study of the companion cases where viscoelastic fluid motion is naturally induced through the application of vibrations, i.e., *thermovibrational* convection. Surprisingly, with the exception of a few studies (Refs. 22 and 23) where thermovibrational flow in viscoelastic fluids was investigated in conjunction with the presence of standard gravitational (buoyancy) convection, no research has been intentionally dedicated to the purely vibrational case (i.e., microgravity conditions).

In order to fill this gap, through this research study, many questions will be tackled on aspects as varied as: the role played by the

relative importance of (vibrationally induced) buoyancy and viscous effects, the relationship between the emerging flow and the frequency of vibrations, the outcomes produced by an increase in the level of elasticity, and, last but not least, the onset of possible instabilities inducing a change in the dominant pattern.

A vast related literature exists for the case of Newtonian fluids (see, e.g., Refs. 24–33). It is known that this kind of convection can develop a non-zero time-averaged velocity in addition to the fluctuating field induced by the imposed forcing. While for small frequency and high amplitude of the vibrations, the purely oscillatory component of the fluid velocity is prevalent, the relative importance of this component and the (time-averaged) velocity is reversed in the opposite situation. This property leads to the remarkable possibility to address the problem in the framework of a potential flow theory. Indeed, many investigators have used this strategy over the years to determine the time-averaged component of velocity "directly," i.e., with no need to account at the same time for fluctuating contributions. This approach is generally known as the "Gershuni formulation."[34]

In general, the interest of investigators in time-averaged quantities has a precise rationale. These can have undesired effects on experiments conducted in the microgravity environment.[35,36] In particular, using the Gershuni's approach, it has been revealed that different solutions can be produced even if a configuration as simple as a square cavity is considered. For instance, for relatively small values of the so-called *Gershuni number* (formally defined in the next section), a stable *quadrupolar* cells pattern initially occurs. On increasing this parameter, however, the system bifurcates from the quadrupolar roll configuration to a stable flow structure (*inversional symmetry* pattern) resulting from the merging of two of the four initial cells along a diagonal direction (see, e.g., Refs. 32 and 37 and 29–31). It is also worth mentioning that, if the assumption of high-frequency (Gershuni regime) is not applicable, the system can respond to the applied forcing in different ways, namely, in a *synchronous*, or *half sub-harmonic* or *non-periodic* way, as described in Refs. 28 and 38.

In a certain way, the present analysis should be regarded as an extension of the line of inquiry about thermovibrational effects in complex fluids started in past works of the present authors.[39–43] More specifically, we address now the case in which the vibrated non-isothermal fluid is viscoelastic.

Following a common practice in the previous literature about buoyancy convection in closed cavities, we consider this problem in the simplified framework represented by a two-dimensional (2D) configuration, leaving to later studies the task of assessing three-dimensional effects through focused comparisons with dedicated 3D simulations. In particular, here, special emphasis is given to the triadic relationship among the three distinct temporal scales involved in these phenomena, namely, the characteristic times related to the diffusion of heat and the relaxation of viscoelastic stresses, and the additional scale dictated by the peculiar nature of the considered flow, i.e., the frequency of "forcing." As using a simplified formulation such as that originally introduced by Gershuni might filter out the physical effects residing on small temporal scales, the overarching equations are solved in their complete non-linear and time-dependent form, as illustrated in Sec. II.

II. MATHEMATICAL MODEL

A two-dimensional (2D) square cavity having lateral no-slip and adiabatic walls ($\partial T / \partial \mathbf{n}|_{\text{wall}} = \mathbf{0}$) and with a fixed difference of temperature between the top and bottom no-slip walls is considered. In order to disentangle the intricacies illustrated in the Introduction, the analysis is performed for both Newtonian and viscoelastic fluids. This problem is summed up in Fig. 1. The direction of the vibrations $\hat{\mathbf{n}}$ is fixed and orthogonal to the temperature gradient ∇T. A convenient way to take into account the vibrations[39–43] is to approximate them as a sinusoidal displacement, i.e.,

$$\mathbf{s}(t^*) = b \sin(\omega t^*)\hat{\mathbf{n}}, \tag{1}$$

where b is the amplitude and ω is the angular frequency ($\omega = 2\pi f$). From this displacement, the corresponding acceleration can be derived by considering its second derivative with respect to time,

$$\mathbf{a}_\omega(t^*) = \gamma \sin(\omega t^*), \tag{2}$$

where $\gamma = -b\omega^2 \hat{\mathbf{n}}$.

Given these premises, the equations governing fluid motion can be written in dimensional form by using the *Boussinesq approximation* as

$$\nabla \cdot \mathbf{u}^* = 0, \tag{3}$$

$$\rho \frac{\partial \mathbf{u}^*}{\partial t^*} + \rho \nabla \cdot (\mathbf{u}^* \mathbf{u}^*) = -\nabla p^* + \eta_s \nabla^2 \mathbf{u}^* + \nabla \cdot \tilde{\boldsymbol{\tau}}^*$$
$$+ \rho \beta_T (T - T_{\text{ref}}) \mathbf{a}_\omega(t^*) \quad , \tag{4}$$

$$\frac{\partial T^*}{\partial t^*} = -\nabla \cdot (\mathbf{u}^* T^*) + \alpha \nabla^2 T^*, \tag{5}$$

where t^* is the time, $\mathbf{u}^*$ is the velocity, T^* is the temperature, p^* is the pressure, $\tilde{\boldsymbol{\tau}}^*$ is the extra-stress tensor due to the viscoelastic effect, ρ is the density of the fluid, η_s is the dynamic viscosity of the solvent (for Newtonian fluids $\eta_s = \eta$ simply represents the dynamic viscosity of the liquid), β_T is the thermal expansion coefficient, and α is the thermal diffusivity. The symbol $(^*)$ is used to highlight that the quantities are *dimensional*.

Although the set of Eqs. (3)–(5) accounts for the main physical quantities characterizing fluid convection (mass, momentum, and energy), however, they do not represent a mathematically closed problem; indeed, they lack a relationship between the viscoelastic stress tensor $\tilde{\boldsymbol{\tau}}^*$ and the velocity, which must therefore be introduced separately.

In the literature, plenty of these models can be found, for instance, the Maxwell, Giesekus, Leonov, Oldroyd-B, FENE-CR (Chilcott–Rallison variant of the so-called finitely extensible nonlinear elastic approach), and many other variants. In particular, for thermal convection problems in viscoelastic fluids, the Oldroyd-B model has
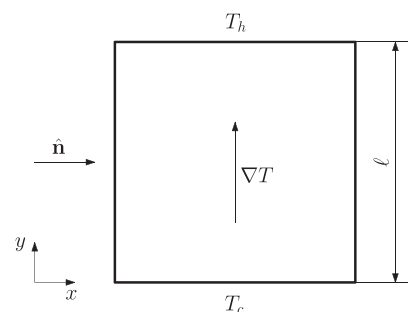

FIG. 1. Sketch of the geometry and schematization of the problem.

enjoyed a widespread use for the development of linear stability analyses (LSA) and the implementation of other numerical methods able to account for non-linear effects (see, e.g., Refs. 16, 19, 22, 23, and 44). Although the Oldroyd-B is actually at the root of most of the recent studies on thermal convection in viscoelastic fluids, however, it is affected by a well-known problem, that is, it has an infinite extensional viscosity. This not only can lead to unphysical behaviors but also pose numerical challenges in specific circumstances (Refs. 45–50). This is the main reason for which this study has entirely been based on the FENE-CR model.[51,52] By replacing the linear Hook law with a finite extensible non-linear spring, this paradigm has already proven to give good results for the case of pure thermogravitational convection (see Ref. 18) as well as to be stable over a wide range of parameters. The improved versatility of this model goes some way to explain its substantial recent development and utilization. The related equation for the temporal evolution of the extra-stress tensor in its dimensional form can be cast in the form:

$$\lambda\left(\frac{\partial\tilde{\tau}^*}{\partial t^*}+\mathbf{u}^*\cdot\nabla\tilde{\tau}^*\right)+f(\mathrm{tr}(\tilde{\tau}^*))\tilde{\tau}^*$$
$$=\eta_p f(\mathrm{tr}(\tilde{\tau}^*))(\nabla\mathbf{u}^*+(\nabla\mathbf{u}^*)^\top)$$
$$+\lambda(\tilde{\tau}^*\cdot\nabla\mathbf{u}^*+(\nabla\mathbf{u}^*)^\top\cdot\tilde{\tau}^*),\tag{6}$$

where $f(\mathrm{tr}(\tilde{\tau}))$ is a quantity related to the possible deformation of the polymeric molecule and reads

$$f(\mathrm{tr}(\tilde{\tau}^*))=\frac{L^2+\frac{\lambda}{\eta_p}\mathrm{tr}(\tilde{\tau}^*)}{L^2-3},\tag{7}$$

where η_p is the dynamic viscosity of the polymer, λ is the so-called *relaxation time,* and L^2 is the so-called *finite extensibility* parameter of the polymer molecule.

Other relevant physical parameters are the *total dynamic viscosity* of the viscoelastic fluid $\eta_0=\eta_s+\eta_p$ and the *solvent-to-total* viscosity ratio $\xi=\eta_s/\eta_0$.

The overarching closed set of balance equations can be put in non-dimensional form using the side ℓ of the square cavity as reference length, α/ℓ for the velocity, ℓ^2/α for the time, α/ℓ^2 for the frequency, $\rho\alpha^2/\ell^2$ for the pressure, $\Delta T=T_h-T_c$ for the temperature, and $\rho\nu_s\alpha/\ell^2$ for the extra-stress tensor $\tilde{\tau}^*$. In the last scaling factor, ν_s is the kinematic viscosity of the Newtonian solvent ($\nu_s=\eta_s/\rho$).

Accordingly, the non-dimensional balance equations in their time-dependent non-linear form read

$$\nabla\cdot\mathbf{u}=0,\tag{8}$$

$$\frac{\partial\mathbf{u}}{\partial t}=-\nabla p-\nabla\cdot(\mathbf{u}\mathbf{u})+Pr\nabla^2\mathbf{u}+Pr\nabla\cdot\tilde{\tau}$$
$$-Pr_g Ra_\omega T\sin(\Omega t)\hat{\mathbf{n}},\tag{9}$$

$$\frac{\partial T}{\partial t}=-\nabla\cdot(\mathbf{u}T)+\nabla^2 T,\tag{10}$$

$$\vartheta\left(\frac{\partial\tilde{\tau}}{\partial t}+\mathbf{u}\cdot\nabla\tilde{\tau}\right)+f(\mathrm{tr}(\tilde{\tau}^*))\tilde{\tau}$$
$$=\zeta f(\mathrm{tr}(\tilde{\tau}^*))(\nabla\mathbf{u}+(\nabla\mathbf{u})^\top)$$
$$+\vartheta(\tilde{\tau}\cdot\nabla\mathbf{u}+(\nabla\mathbf{u})^\top\cdot\tilde{\tau}).\tag{11}$$

The non-dimensional groups that appear in these equations are the Prandtl number for the Newtonian solvent $Pr=\nu_s/\alpha$, the

non-dimensional frequency $\Omega=\ell^2\omega/\alpha$, the generalized Prandtl number $Pr_g=Pr/\xi$, the elasticity number $\vartheta=\lambda\alpha/\ell^2$, the viscosity ratio $\zeta=\eta_p/\eta_s=(1-\xi)/\xi$, and the vibrational Rayleigh number,

$$Ra_\omega=\frac{b\omega^2\beta_T\Delta T\ell^3}{\nu_0\alpha},\tag{12}$$

where $\nu_0=\eta_0/\rho$ is the total kinematic viscosity. This expression can be seen as an alternate form of the classical Rayleigh number, where in place of the classical steady gravitational acceleration, the amplitude of the considered monochromatic periodic acceleration is used. Moreover, for the sake of clarity, it is worth highlighting that the parameter ϑ, which is referred to in this work as *elasticity number*,[16,18,19] is analogous to the so-called *Deborah number*.[20]

We also introduce a new non-dimensional quantity, that is, the ratio of the relaxation time λ (the characteristic time of the polymer molecules dynamics) and the period of the oscillations T_ω^* ($T_\omega=2\pi/\Omega$, i.e., the characteristic time of the external dynamic force),

$$\Sigma=\frac{\lambda}{T_\omega^*}=\frac{\vartheta\Omega}{2\pi}.\tag{13}$$

Furthermore, following the traditional approach used in the field of thermovibrational flows, we split the fluid velocity into a time-average component $\mathbf{u}_{\mathrm{mean}}$ and a periodic component that oscillates at the same frequency of the imposed vibrational disturbances ($\mathbf{u}'=\mathbf{u}-\mathbf{u}_{\mathrm{mean}}$), where

$$\mathbf{u}_{\mathrm{mean}}=\frac{1}{T_\omega}\int_{T_\omega}\mathbf{u}(t)\,dt.\tag{14}$$

The temperature and the viscoelastic stress fields are decomposed accordingly. In such a context, it is also worth recalling that the intensity of the average field is directly related to another non-dimensional parameter known in the literature as the *Gershuni number*,[29]

$$Gs=\frac{(b\omega\beta_T\Delta T\ell)^2}{2\nu_0\alpha}=\left(\frac{Ra_\omega}{\Omega}\right)^2\frac{Pr_g}{2}.\tag{15}$$

As shown in Refs. 39–42, typically, $\mathbf{u}_{\mathrm{mean}}$ and $\mathbf{u}'$ scale with Gs and Ra_ω, respectively.

III. NUMERICAL METHOD

The balance Eqs. (8)–(11) have been integrated over the domain through an algorithm that belongs to the category of the so-called projection methods.[53–56] In particular, openFOAM® relies on the so-called *PISO* (Pressure-Implicit with Splitting of Operators) method and the related Rhie and Chow[57] interpolation scheme, which allows the set of mixed parabolic and hyperbolic balance equations to be solved on a *co-located* grid.

Moreover, a standard Second-Order Upwind Difference Scheme (SOUDS) has been used for the spatial discretization of the convective terms of the momentum and energy equation, while a Central Difference Scheme (CDS) stencil, yet accurate to the second-order, has been implemented for the diffusive terms. Special attention has been paid to the solution of Eq. (11). In particular, in place of the SOUDS scheme, a Midmod variant has been chosen for the discretization of the convective terms. This approach has guaranteed good performances over a wide range of parameters and good agreement with test

cases. Moreover, to mitigate the numerical singularities mentioned in Sec. II, in line with the methodology proposed by Favero et al.,[58] Eq. (9) has been implemented numerically as

$$\frac{\partial \mathbf{u}}{\partial t} + \nabla \cdot (\mathbf{uu}) - Pr(1+\zeta)\nabla^2\mathbf{u}$$
$$= -\nabla p - Pr\zeta\nabla^2\mathbf{u} + Pr\nabla \cdot \tilde{\boldsymbol{\tau}} - Pr_g Ra_\omega T \sin(\Omega t). \quad (16)$$

Put simply, two diffusive terms having similar "weight" and meaning by a mathematical point of view have been introduced at the left and right hand sides of this equation. Nonetheless, one has been numerically treated in an implicit way while the other one has been implemented explicitly. In this way, some artificial numerical diffusivity, quantitatively negligible, has been introduced in the time-marching procedure, in order to increase appreciably the "ellipticity" of the momentum equation and improve the numerical stability of the solver accordingly. This methodology is known in the literature as *DEVSS* (Discrete Elastic-Viscous-Split-Stress) method.[59]

A. Validation

The viscoelastic kernel of the computational platform described in the preceding sections was already validated by Lappa and Boaro[18] in the framework of a multi-stage approach by considering different types of convection and fluid-dynamic instabilities. Both fundamental situations where the emerging instability has a purely elastic nature (isothermal liquids) or a thermal origin (overstable Rayleigh-Bénard convection) were examined and good agreement was found with the existing literature on these subjects. In particular, the reader is referred to Table I for what concerns the outcomes of the comparison with the LSA by Martínez-Mardones and Pérez-García[60] for the onset of standard Rayleigh-Bénard convection in a layer of Oldroyd-B fluid delimited by top and bottom *solid* walls with $Pr_g = 10$, $\xi = 0.5$, and $\vartheta = 0.1$. The present results have been obtained using a structured mesh (2D simulation) with 4500 nodes and a domain having non-

TABLE I. Comparison with the linear stability analysis by Martínez-Mardones and Pérez-García [60]. (a) Non-dimensional angular frequency $\tilde{\omega}$ determined with different models as a function of the Rayleigh number. (b) Non-dimensional angular frequency $\tilde{\omega}$ extrapolated to the critical Ra predicted by the linear stability analysis.

(a)		FENE-CR	
Ra	Oldroyd-B	$L^2 = 10^4$	$L^2 = 10^3$
2500	15.03	15.01	15.00
2200	12.90	12.87	12.60
2000	10.90	10.90	10.90
1900	7.48	7.46	9.63
1800	5.82	5.80	7.50
1775	5.10	5.10	5.65

(b)	
Approach	$\tilde{\omega}$
FENE-CR ($L^2 = 10^3$)	4.93
FENE-CR ($L^2 = 10^4$)	4.85
Oldroyd-B	4.74
Linear Stability Analysis	4.63

dimensional horizontal extension 15 with periodic boundary conditions at the lateral boundaries. The non-dimensional angular frequency of oscillation of the flow $\tilde{\omega}$ has been determined. Then it has been extrapolated to the value of the critical Rayleigh number predicted by the LSA, i.e., $Ra_c \approx 1700$. As evident in this table, the difference between the values predicted by those authors and the present one obtained with the Oldroyd-B model is $\approx 2\%$.

As a next step of such a validation hierarchy, given the specific topic considered in this work, we have considered gravitationally modulated viscoelastic convection. Relevant information on such a benchmark has been sourced from the study by Lyubimova and Kovalevskaya,[23] where the authors applied a LSA technique to investigate the onset of Rayleigh-Bénard convection in a horizontal layer of Oldroyd-B fluid delimited by top and bottom *stress-free* walls under the effect of a time-periodic acceleration $\mathbf{a}_\omega(t)$ added to the steady gravitational acceleration $\mathbf{g}$. In particular, these authors modeled such additional acceleration as a square wave superimposed on a steady value, that is,

$$\mathbf{a}_\omega(t^*) = \gamma\tanh(10\sin(\omega t^*)), \quad (17)$$

which leads to express the buoyancy term appearing in the momentum equation (in dimensional and in non-dimensional form, respectively) as

$$\mathbf{B}(t^*) = \rho g\beta(T^* - T_0^*)(1 + \frac{b\omega^2}{g}\tanh(10\sin(\omega t^*)))\hat{\mathbf{i}}_g \quad (18)$$

and

$$\mathbf{B}(t) = RaT(1 + \Gamma\tanh(10\sin(\Omega t)))\hat{\mathbf{i}}_g, \quad (19)$$

where Ra is the classical Rayleigh number based on the steady gravitational acceleration, $\Gamma = b\omega^2/g$ is the non-dimensional amplitude of the oscillatory acceleration, and $\hat{\mathbf{i}}_g$ is the unit vector along the direction of the gravitational acceleration.

Moreover, the *free-free* boundary condition originally used by Lyubimova and Kovalevskaya[23] for the top and bottom boundary has been implemented here as follows:

$$\left[((\nabla\mathbf{u}) + (\nabla\mathbf{u})^\top) + \tilde{\boldsymbol{\tau}}\right] \cdot \hat{\mathbf{n}}_B = 0, \quad (20)$$

where $\hat{\mathbf{n}}_B$ is the unit vector perpendicular to the boundary.

For $Pr_g = 7$, $\Omega = 26.5$, $\Gamma = 1$, $\xi = 0.1$, and $\vartheta = 0.06$, Lyubimova and Kovalevskaya[23] found a critical value of the Rayleigh number for the onset of buoyancy convection $Ra_c \approx 470$. Following the approach already undertaken by Lappa and Boaro,[18] the present computations have been performed using both the Oldroyd B (originally employed by these authors) and the FENE-CR assuming different values of the parameter L^2, namely, $L^2 = 1000$ and $L^2 = 200$. We wish to recall that the latter is a typical value used in most of the existing literature based on this model; accordingly, it has also been employed in this work to produce the results presented in Sec. IV. The data shown in Table II have been obtained using a structured mesh (2D simulation) with 4500 nodes and a domain having non-dimensional horizontal extension 15 with periodic boundary conditions at the lateral boundaries. In particular, in order to mimic the typical modus operandi at the basis of LSA, we have determined the non-dimensional amplitude A of the unsteady convective state for

TABLE II. Comparison with the linear stability analysis by Lyubimova and Kovalevskaya.[23] (a) Non-dimensional amplitude of oscillation A determined with different models as a function of the Rayleigh number. (b) Critical Rayleigh number Ra_c extrapolated for $A = 0$.

(a)

Ra	Oldroyd-B	FENE-CR	
		$L^2 = 10^4$	$L^2 = 10^3$
530	6.52	6.51	6.52
560	8.31	8.31	8.31
590	11.96	11.96	11.90
620	12.99	12.94	13.07

(b)

Approach	Ra_c
FENE-CR ($L^2 = 200$)	469
FENE-CR ($L^2 = 10^4$)	473
Oldroyd-B	472
Linear Stability Analysis	470

different values of Ra [Table II(a)] and then we have computed Ra_c through (quadratic) extrapolations of A to 0 [Table II(b)]. As quantitatively substantiated by these tables, the agreement between the present results and those yielded by LSA is excellent. Interestingly, these tables demonstrate that the overall mathematical and numerical treatment underpinning the present work is *consistent*, i.e., as the finite extensibility parameter of the polymer molecule L^2 increases, the results calculated with the FENE-CR constitutive equation tend to those obtained with the Oldroyd-B (as expected).

B. Mesh refinement study

The balance equations have been discretized on a Cartesian grid having the same number of divisions in each direction. For the grid refinement, we have considered as control parameters the amplitude (A_{u_y}) and the frequency (Ω_{u_y}) of the y component of $\mathbf{u}_{\text{mean}}$ signal measured with two virtual probes located in the center and in the north-west corner of the cell, respectively, assuming a viscoelastic fluid with $Pr_g = 10$, $Gs = 5 \times 10^2$, $\Omega = 10^2$, $Ra_\omega = 10^3$, and $\vartheta = 0.1$ ($\Sigma = 1.6$). As witnessed by the results in Table III, a mesh having 80 cells in each direction is sufficient to ensure grid-independent solutions, which explains why we have used this resolution for all the cases described in Sec. IV.

IV. RESULTS

As already explained to a certain extent in the Introduction, this study aims to carry out a parametric analysis of the thermovibrational problem in a square cavity filled with a FENE-CR fluid and compare the results with those obtained for a Newtonian liquid under the same conditions. Toward this end, without loss of generality, we set $Pr_g = 10$ (this value being representative of a large class of high-Pr "Boger fluids," known for their ability to retain an essentially constant viscosity over a wide range of shear rates, see, e.g., Refs. 16 and 18); obviously, for a Newtonian fluid $Pr_g = Pr$ since it does not have a polymeric component.

TABLE III. Mesh refinement study. Case $Pr_g = 10$, $Gs = 5 \times 10^2$, $\Omega = 10^2$, $Ra_\omega = 10^3$, $\vartheta = 0.1$, $\Sigma = 1.6$, viscoelastic fluid. Presented data relate to probes located in the center of the cell (1/2,1/2), and in the point (1/8,7/8) (the "corner").

Mesh	Center		Corner	
	A_{u_y}	Ω_{u_y}	A_{u_y}	Ω_{u_y}
20×20	0.014 9	0.192	0.003 2	0.194
40×40	0.015 4	0.197	0.003 5	0.193
60×60	0.015 6	0.197	0.003 1	0.195
80×80	0.015 7	0.196	0.003 3	0.195
100×100	0.015 8	0.195	0.003 1	0.195

Moreover, we consider a viscoelastic fluid having $\xi = 0.5 \to \zeta = (1 - \xi)/\xi = 1$ and $L^2 = 200$. Due to the high-dimensional nature of the space of parameters that characterizes this problem, we systematically vary one parameter while the other independent non-dimensional groups are kept constant. Notably, in the absence of observational information to properly constrain the model parameters, such an approach is instrumental in revealing the "process controlling factors."

A. Preliminary analysis of the Newtonian problem

Most conveniently, in the frame of the above-mentioned step-by-step approach, we analyze initially the effect of the Gershuni number on the pattern evolution of $\mathbf{u}_{\text{mean}}$ for a Newtonian fluid. More specifically, we fix the value of the angular frequency to $\Omega = 10^2$ and vary Ra_ω in order to have Gs spanning the range of orders of magnitude from $O(10^2)$ to $O(10^7)$. In this regard, we start from the observation that, in general $[Gs > O(10^2)]$, the mean-field is not steady, but exhibits an oscillatory behavior. A first example of such dynamics for the initial sub-range of Gs going from $O(10^3)$ to $O(10^4)$ is depicted in Fig. 2.

The aforementioned inversional symmetry pattern can be distinguished there, i.e., two small cells are located in opposite corners of the cavity while a big central vortex, stretched along the diagonal of the square, occupies almost the entire domain [Fig. 2(a)]. This diagonal direction represents a symmetry plane for the pattern. As revealed by the sequence of snapshots, however, as time passes, the eddies located in the corners keep expanding until the four cells with comparable diameter, representing the aforementioned "quadrupolar field," are formed. At this stage, a new process is enabled by which two cells of this configuration progressively undergo coalescence until a condition similar to the one represented in the initial snapshot is recovered. The cells in the corners eventually grow again until the intermediate state with the quadrupolar field re-appears. This process is characterized by a period (hereafter denoted by T_{umean}) much larger than the period of the forcing (i.e., $T_{\text{umean}} \gg T_\omega$).

Figure 3 shows the corresponding total velocity field. As the reader will realize by taking a look at this sequence, the flow essentially consists of a main roll that changes periodically its sense of circulation (from the clockwise to the counterclockwise sense and vice versa within the forcing period T_ω). In some snapshots, smaller rolls nucleating inside the main circulation can be seen.
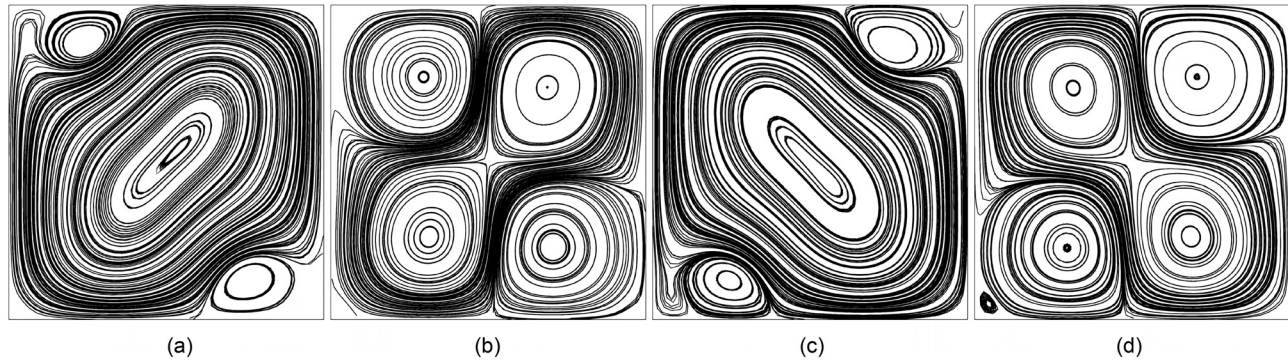
FIG. 2. Streamlines of $\mathbf{u}_{\text{mean}}$, $Pr = 10$, $Gs = 5 \times 10^2$, $\Omega = 10^2$, and $Ra_\omega = 10^3$. Thermovibrational convection in Newtonian fluid. Four snapshots equally spaced in time within the oscillation period $T_{\text{umean}} \cong 30$. (a) $t_0 = 39.6$, (b) $t = t_0 + (1/4)T_{\text{umean}}$, (c) $t = t_0 + (1/2)T_{\text{umean}}$, and (d) $t = t_0 + (3/4)T_{\text{umean}}$.

Notably, these behaviors should be interpreted as the result of the superposition of convective modes with different symmetries. Relevant information along these lines can be found, e.g., in the study by Mizushima.[61] Although that analysis was entirely focused on classical Rayleigh-Bénard (RB) convection, the considerations elaborated there are relatively general and can, therefore, be applied also to the circumstances considered in this work.

In general, the distinct modes of convection allowed in a specific geometry can be identified *a priori* on the basis of the various possible symmetries that can be retained or broken by the emerging flow. For the square cavity, these are obviously the reflection with respect to the *x* axis in Fig. 1, i.e., the symmetry with respect to the direction of the imposed vibrations, and the analogous reflection property with respect to the vertical cavity centerline, i.e., the direction of the applied temperature gradient. The combination of these two properties can produce an additional possible solution, characterized by an even higher degree of symmetry, that is the flow satisfying the so-called *centro-symmetry*; this makes the square geometry an ideal target to study many concurrent aspects. On the basis of these relatively simple arguments partially based on the earlier analysis by Mizushima,[61] the set of possible modes relevant to the present problem can immediately be partitioned into four fundamental classes (see Fig. 4), namely:

(aa): The antisymmetric-antisymmetric mode. Both the *x*-symmetry and *y*-symmetry are broken in this case, the flow typically displaying an odd number of rolls along both directions.

(sa): The symmetric-antisymmetric mode. Only the symmetry with respect to the (vertical) *y* axis is retained, the flow being typically characterized by an even number of rolls along the *x* and an odd number of rolls along *y*.

(as): The antisymmetric-symmetric mode. Only the symmetry with respect to the (horizontal) *x* axis is retained, the flow being typically characterized by an odd number of rolls along the *x* and an even number of rolls along *y*.

(ss): The symmetric-symmetric mode. This mode has an even number of vortex cells along both the *x* and *y* axes. It gives rise to a centro-symmetric configuration when the number of rolls along both the *x* and *y* directions is the same and to a columnar arrangement if the number of rolls along *y* is larger.

Although for standard RB convection, one mode only is generally selected at the onset, it is known that the combination of different modes excited at the same time for relatively high values of the control parameter (the standard Rayleigh number) can lead to more complex patterning behaviors. As an example, Mizushima and Adachi[62] found the diagonal mode, i.e., the pattern with the central extended roll that seems to tilt to one side under the influence of the smaller vortices, to
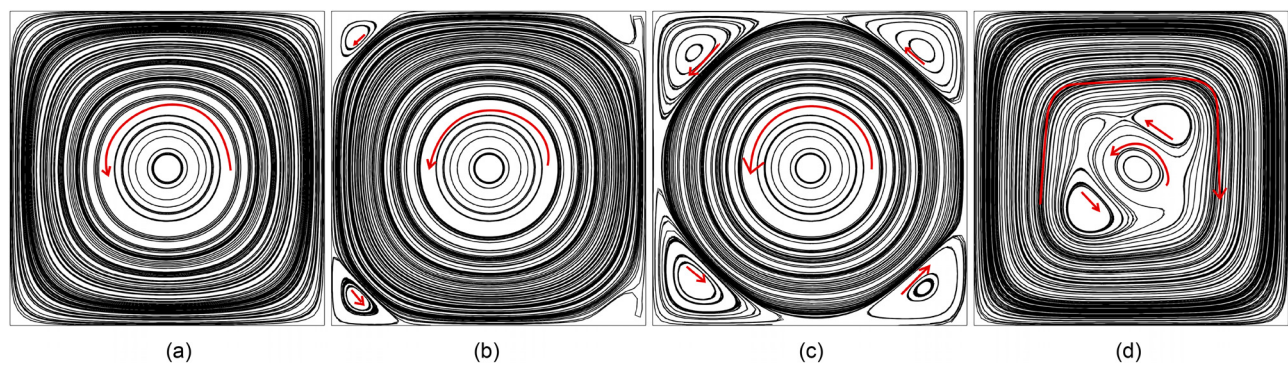

FIG. 3. Streamlines of the total velocity $\mathbf{u}$, $Pr = 10$, $Gs = 5 \times 10^2$, $\Omega = 10^2$, and $Ra_\omega = 10^3$. Thermovibrational convection in Newtonian fluid. Details of the inversion of the central cell in the neighborhood of $T_\omega/4$. (a) $t = 0.28$, (b) $t = 0.2838$, (c) $t = 0.284$, and (d) $t = 0.2848$.
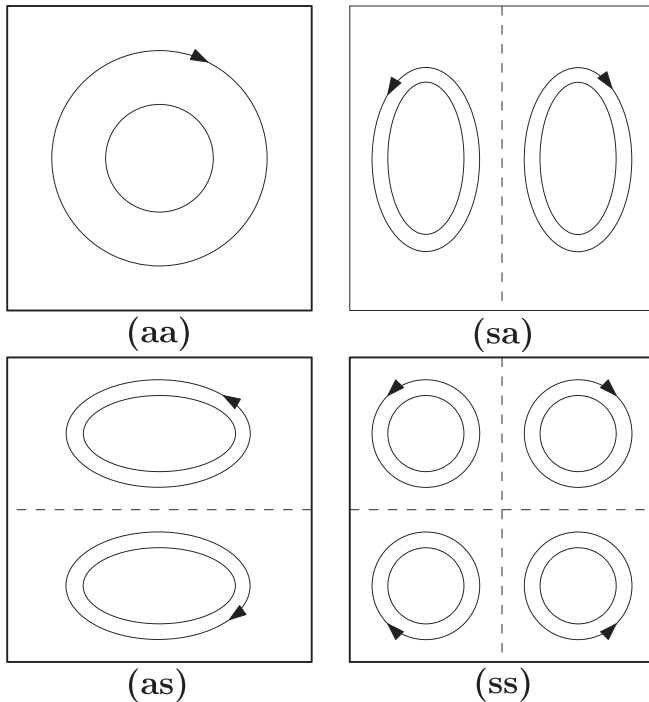
FIG. 4. Categorization of possible solutions of buoyancy convection in 2D finite enclosures in terms of related symmetries. (aa): antisymmetric-antisymmetric mode, (sa): symmetric-antisymmetric mode, (as): antisymmetric-symmetric mode, and (ss): symmetric-symmetric mode.

be produced as a result of the interplay of more fundamental modes [(**aa**) + (**ss**)]. Similar results were also reported in the study on RB convection by Lappa[63] where a sequence of events like that depicted in Fig. 2 was found for relatively high values of Ra ($Ra = 5 \times 10^5$ for $Pr = 15$).

This way of categorizing different solutions on the basis of the number and location of rolls is extremely useful; it is generally regarded as "a spatial perspective" for flow interpretation, an application of what is generally known as "vorticity thinking." In the light of these

propaedeutical arguments, the stages of evolution reported in Fig. 2 can therefore be seen as the superposition or competition of fundamental modes of time-averaged convection with different symmetries.

As witnessed by Fig. 5, however, an increase in Ra_ω can induce a change in the time-averaged streamlines distribution ($Gs = 1.01 \times 10^5$). Some of the features visible in the previous Fig. 2 can still be clearly recognized; as an example, by comparing Figs. 2(a) and 5(a) it becomes evident that, though the considered increase in Ra_ω affects the minimum size of the smaller cells located in the corners, the diagonal directions still play the role of symmetry planes. Nevertheless, interestingly, new features show up during the evolution. These are very evident in Fig. 5(b), where four small cells pop up in proximity to the lateral adiabatic walls (two for each side). Apart from these details, however, the evolution is quite similar to the one discussed for the previous case.

As qualitatively illustrated in Fig. 6, other morphological changes become effective on further increasing Ra_ω ($Gs = 2.75 \times 10^5$). The two opposing couples of newly formed cells adjacent the adiabatic walls have now a size that is comparable to that of the corner cells [Fig. 6(b)]. Although the dynamics are still similar to those described for $Gs = 5 \times 10^2$, as an important distinguishing mark, the big central cell is taken over by an involved circulation system encompassing a zig-zag-shaped arrangement of (four) smaller cells [see Fig. 6(a)].

The spatiotemporal scenario consists essentially of the alternation of a configuration with eight distinct time-averaged rolls regularly arranged in two vertical columns and four horizontal rows, i.e., a (**ss**) configuration [Figs. 6(b) and 6(d)] and two intermediate patterns where one cell of each row contributes to the formation of a zig-zag shaped circulation system pervasive throughout the cavity [Figs. 6(a) and 6(c) being one the mirror image of the other]. Hereafter, we will refer to these patterns as the "columnar mode of time-averaged convection."

A further increase in the vibrational Rayleigh number does not affect considerably the dynamic evolution of this mode from a qualitative point of view. However, the cells located in the center of the cavity keep growing until configurations like those shown in Figs. 7(a) and 7(b) are obtained. The cells located close to the adiabatic sides of the cavity become so large that they occupy almost the whole space of the geometry [see Fig. 7(b)].
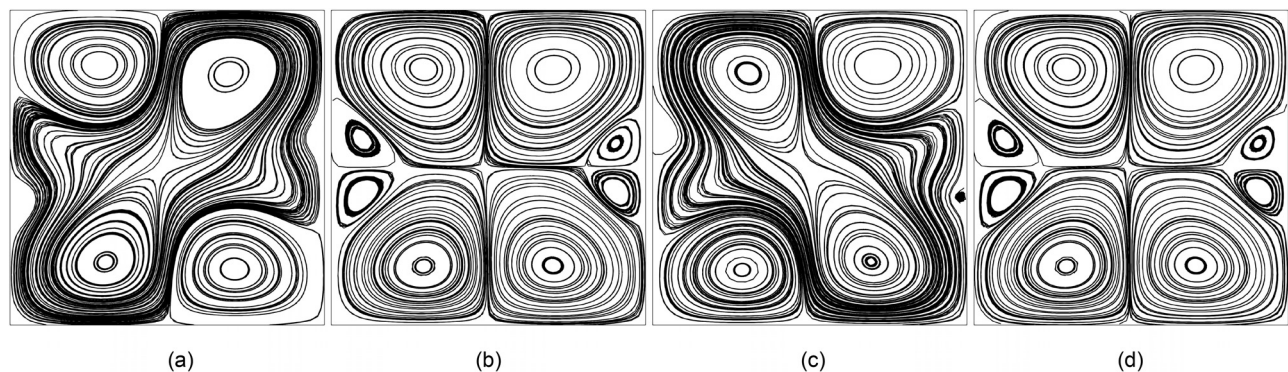

FIG. 5. Streamlines of $\mathbf{u}_{mean}$, $Pr = 10$, $Gs = 1.01 \times 10^5$, $\Omega = 10^2$, and $Ra_\omega = 1.42 \times 10^4$. Thermovibrational convection in Newtonian fluid. Four snapshots equally spaced in time within the oscillation period $T_{umean} \cong 26.8$. (a) $t_0 = 40$, (b) $t = t_0 + (1/4)T_{umean}$, (c) $t = t_0 + (1/2)T_{umean}$, and (d) $t = t_0 + (3/4)T_{umean}$.
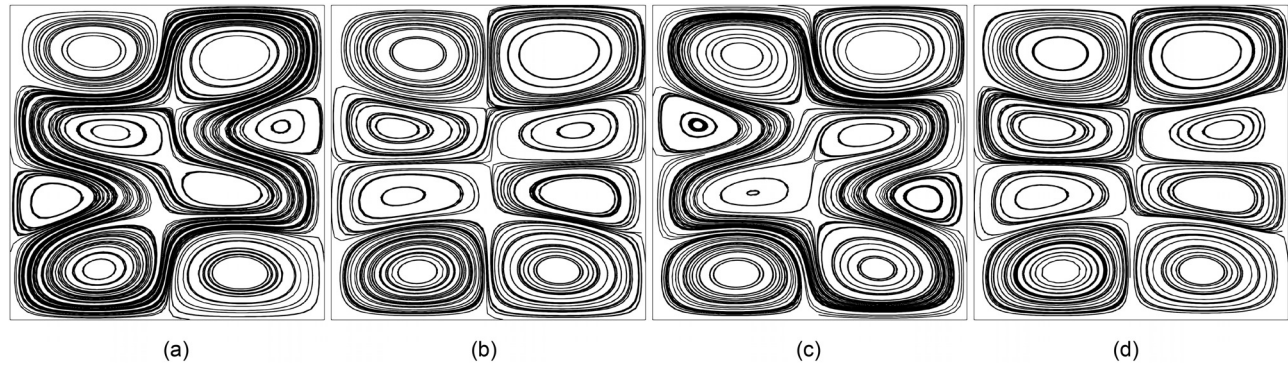
FIG. 6. Streamlines of $\mathbf{u}_{mean}$, $Pr = 10$, $Gs = 2.75 \times 10^5$, $\Omega = 10^2$, and $Ra_\omega = 2.35 \times 10^4$. Thermovibrational convection in Newtonian fluid. Four snapshots equally spaced in time within the oscillation period $T_{umean} \cong 32.1$. (a) $t_0 = 40.2$, (b) $t = t_0 + (1/4)T_{umean}$, (c) $t = t_0 + (1/2)T_{umean}$, and (d) $t = t_0 + (3/4)T_{umean}$.

Before moving to the cases with viscoelastic fluid, as a concluding remark for this section, we wish also to highlight that for not too high values of Ω, (as expected) the problem also sensitively depends on this parameter.

Interestingly, if we increase Ω to 1.5×10^2 keeping Gs constant, the dynamics of the system changes completely. As an example, Fig. 8 shows the streamlines patterning behavior of a fluid with the same value of Gs considered in Fig. 2 ($Gs = 5 \times 10^2$) and a slightly larger value of Ω ($Ra_\omega = 1.5 \times 10^3$ and $\Omega = 1.5 \times 10^2$).

As the reader will easily realize by inspecting this figure, the scenario is different. Initially [Fig. 8(a)] there is a single cell with streamlines having square morphology. However, two smaller cells, located in the north-east and south-west corners, respectively, grow as time passes. Due to this phenomenon, the central cell undergoes a progressive corrugation process that breaks it into eight independent rolls.

This time, however, the time-averaged rolls are not aligned along the direction of the walls; rather they are disposed radially with respect to the center of the cavity, i.e., they satisfy a property of centrosymmetry; therefore, we coin for this regime the denomination of "radial mode of time-averaged convection."

After some time, the central vortex pervasive throughout the cavity forms again; however, in this case, the smaller cells (the eddies) are

located in the north-west and south east corners. Stripped to its basics, this specific phenomenon may therefore be interpreted as the alternation of modes with the **(aa)** and the central symmetry, respectively.

The complexity of the pattern increases as the frequency is set to $\Omega = 1.75 \times 10^2$ (as depicted in Fig. 9). In these circumstances, the initial size of the two eddies mentioned before is bigger than that found for the case with $\Omega = 1.5 \times 10^2$. Moreover, although the evolution mechanism is very similar to the previous one, at a certain stage, four big rolls manifest in the center of the cavity while other four smaller cells are located in pair close to the cold and hot walls, respectively. This state may therefore be regarded as a "hybrid radial-columnar time-averaged mode of convection."

A further increase in Ω to 200 generates a pattern that is basically the same already illustrated in Fig. 2. This solution seems to take the role of preferred mode of convection even for higher values of Ω.

B. The influence of *Gs* for a viscoelastic fluid

Following the same approach undertaken in the previous section, specific numerical examples are conceived and presented to provide inputs for an increased understanding of the mechanisms underlying viscoelastic fluid flow. In order to do so, we fix the frequency to $\Omega = 10^2$ and vary Ra_ω (and therefore Gs). Obviously, in this case, the set of parameters to be considered is richer as it also includes the elasticity number ϑ, which we set initially to $\vartheta = 0.1$ (the corresponding value of Σ being $\Sigma = 1.6$).

Starting again from the case $Gs = 5 \times 10^2$ (the related pattern evolution being depicted in Fig. 10), it can be seen that the initial frames [Figs. 10(a) and 10(b)] look similar to the corresponding ones in Fig. 9 (the aforementioned mixed radial-columnar mode of time-averaged convection); although in this case the lateral eddies nucleate in the north-west and south-east corners, they still manifest themselves in proximity to the adiabatic walls. In particular, comparison of Fig. 9(b) and Fig. 10(b) is instrumental in showing that when the viscoelastic fluid is considered, the streamlines of the main central vortex are more "undulated" with respect to the Newtonian case. The evolution in time is similar to that already illustrated in Fig. 9, but the streamlines display a more complex topology. Indeed, due to the emergence of two new couples of (small) rolls along the hot and cold walls, respectively, a total of twelve cells can be distinguished at a certain stage. Such cells are organized in two columns aligned with the
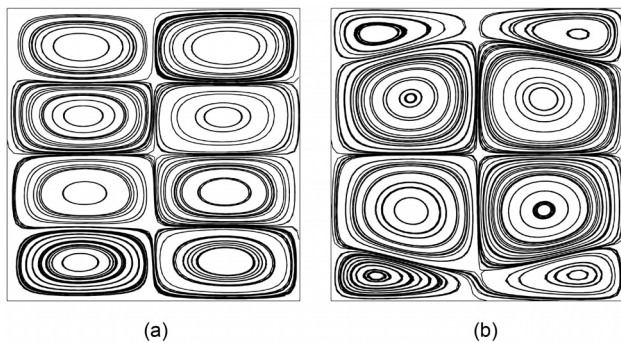

FIG. 7. Streamlines of $\mathbf{u}_{mean}$, $Pr = 10$, $\Omega = 10^2$. Thermovibrational convection in Newtonian fluid. Snapshots to compare to Fig. 6(b). (a) $Gs = 6 \times 10^5$, $Ra_\omega = 3.46 \times 10^4$, $t = 40.8 + (1/4)T_{umean}$, $T_{umean} \cong 32$ and (b) $Gs = 1 \times 10^7$, $Ra_\omega = 1.41 \times 10^5$, $t = 43 + (1/4)T_{umean}$, $T_{umean} \cong 32$.

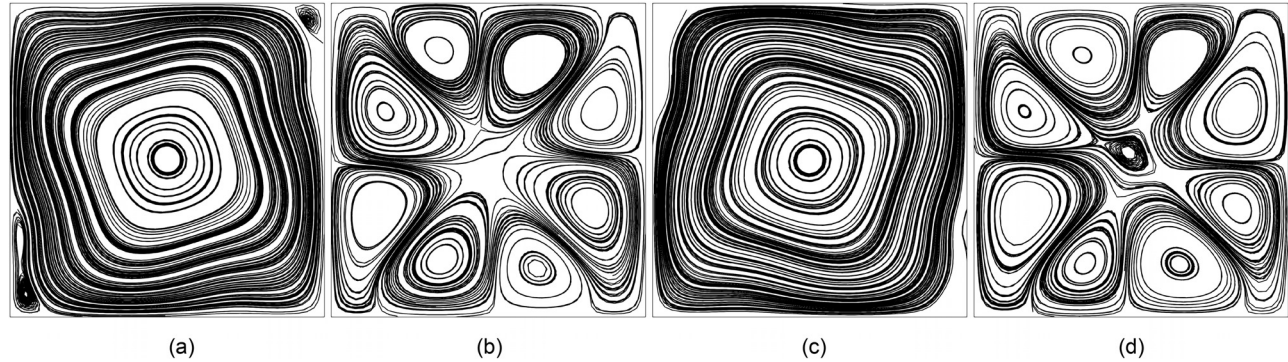**FIG. 8.** Streamlines of $\mathbf{u}_{\text{mean}}$, $Pr = 10$, $Gs = 5 \times 10^2$, $\Omega = 1.5 \times 10^2$, and $Ra_\omega = 1.5 \times 10^3$. Thermovibrational convection in Newtonian fluid. Four snapshots equally spaced in time within the oscillation period $T_{\text{umean}} \cong 22.3$. (a) $t_0 = 26.5$, (b) $t = t_0 + (1/4) T_{\text{umean}}$, (c) $t = t_0 + (1/2) T_{\text{umean}}$, and (d) $t = t_0 + (3/4) T_{\text{umean}}$.

temperature gradient direction. Also in this case, the more spatially extended rolls located in the central area expand and merge until a single main vortex is established again. The second half of the period begins and evolves displaying a qualitatively similar behavior.

In this regard, comparison of Fig. 11 with Fig. 3 is also extremely useful as it reveals the changes induced by viscoelastic effects in the total (instantaneous) velocity. Indeed, it can be seen that in terms of total velocity field, the number of rolls present in the latter case is always larger. This indirectly confirms the increased complexity of the

time-averaged pattern shown in Fig. 10 with respect to that reported in Fig. 2.

For the sake of completeness, Figs. 12 and 13 show the evolution over the forcing period T_ω of selected components of the viscoelastic stress tensor, i.e., the first normal stress and tangential stress, respectively (the second normal stress is not shown as it displays a configuration that appears rotated by 90° with respect to that of the first normal stress). Interestingly, these patterns indicate that the first (second) normal stress generally attains relatively large values in proximity to the
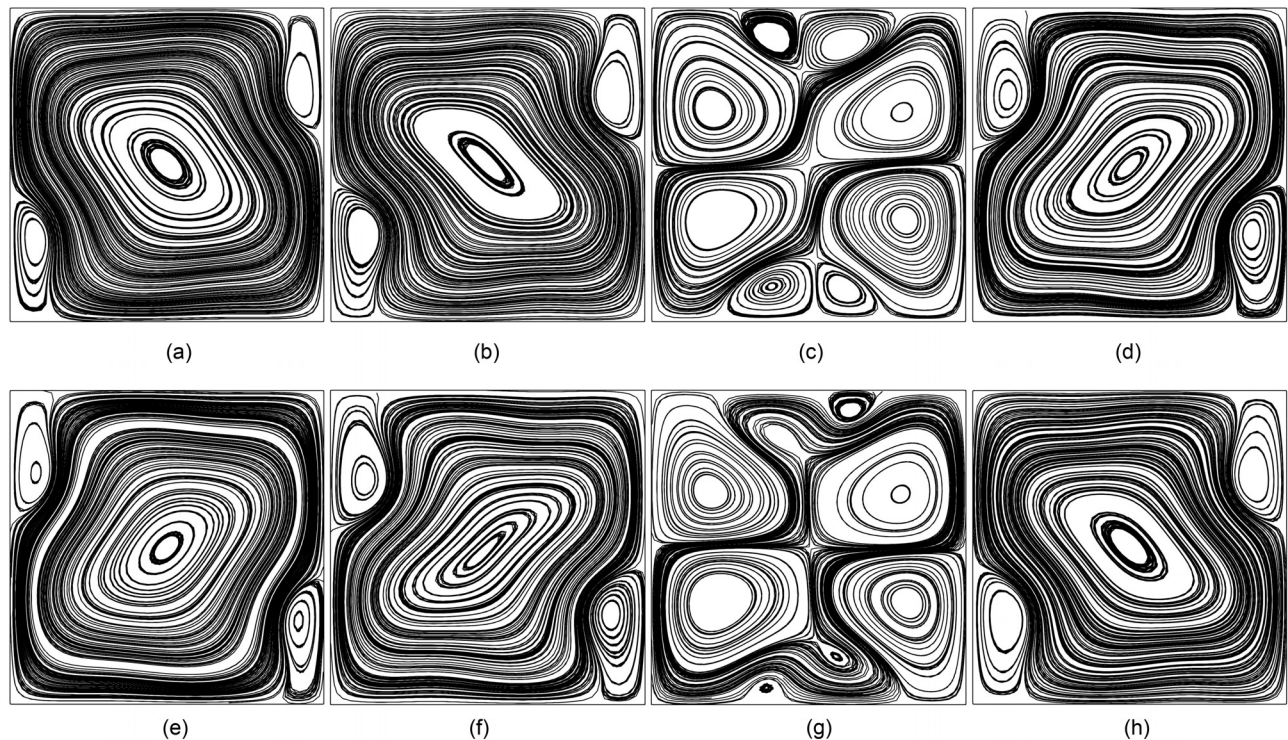

FIG. 9. Streamlines of $\mathbf{u}_{\text{mean}}$, $Pr = 10$, $Gs = 5 \times 10^2$, $\Omega = 1.75 \times 10^2$, and $Ra_\omega = 1.75 \times 10^3$. Thermovibrational convection in Newtonian fluid. Eight snapshots equally spaced in time within the oscillation period $T_{\text{umean}} \cong 18.3$. (a) $t_0 = 22$, (b) $t = t_0 + (1/8) T_{\text{umean}}$, (c) $t = t_0 + (1/4) T_{\text{umean}}$, (d) $t = t_0 + (3/8) T_{\text{umean}}$, (e) $t = t_0 + (1/2) T_{\text{umean}}$, (f) $t = t_0 + (5/8) T_{\text{umean}}$, (g) $t = t_0 + (3/4) T_{\text{umean}}$, and (h) $t = t_0 + (7/8) T_{\text{umean}}$.
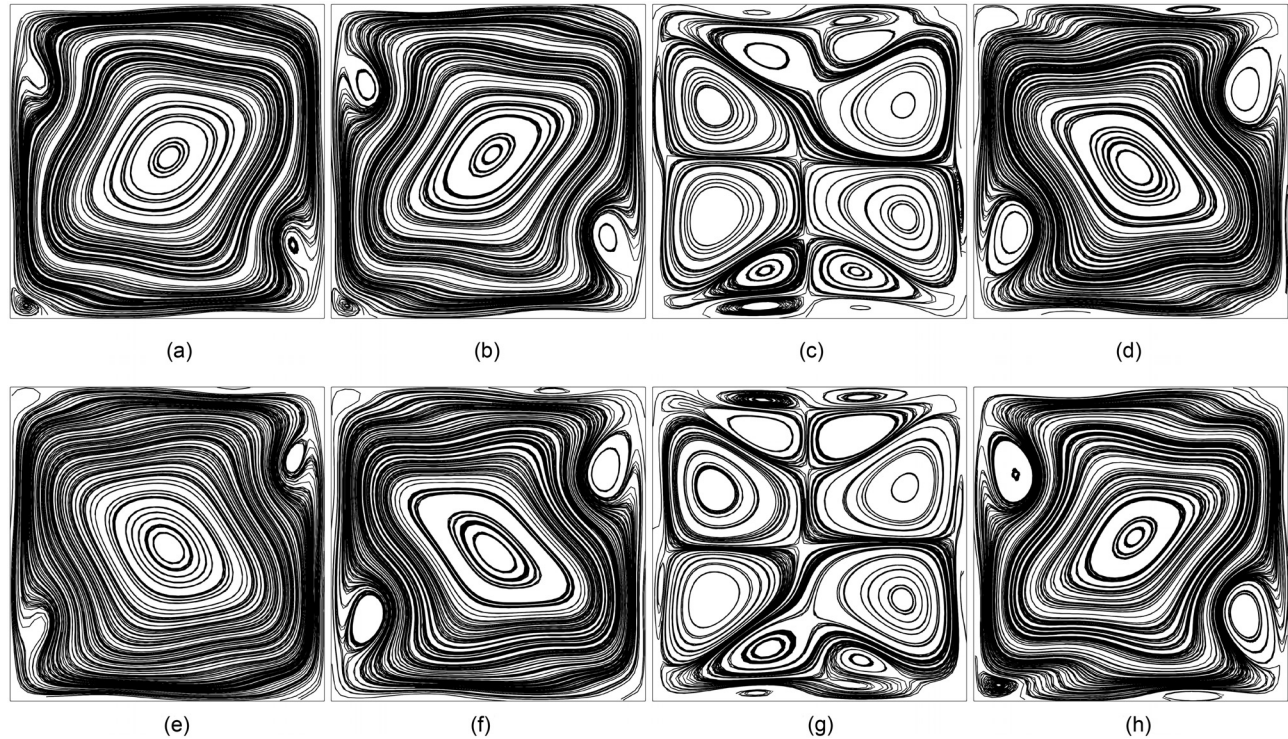
FIG. 10. Streamlines of $\mathbf{u}_{\text{mean}}$, $Pr_g = 10$, $Gs = 5 \times 10^2$, $\Omega = 10^2$, $Ra_\omega = 10^3$, $\vartheta = 0.1$, and $\Sigma = 1.6$. Thermovibrational convection in viscoelastic fluid. Eight snapshots equally spaced in time within the oscillation period $T_{\text{umean}} \cong 32.14$. (a) $t_0 = 39.1$, (b) $t = t_0 + (1/8)T_{\text{umean}}$, (c) $t = t_0 + (1/4)T_{\text{umean}}$, (d) $t = t_0 + (3/8)T_{\text{umean}}$, (e) $t = t_0 + (1/2)T_{\text{umean}}$, (f) $t = t_0 + (5/8)T_{\text{umean}}$, (g) $t = t_0 + (3/4)T_{\text{umean}}$, and (h) $t = t_0 + (7/8)T_{\text{umean}}$.

walls perpendicular (parallel) to the imposed temperature gradient. The corresponding tangential component essentially follows the evolution of the instantaneous velocity field, i.e., it is characterized by regions of positive and negative values adjacent to the solid boundaries, which periodically swap their position within the forcing period. As evident in Fig. 14(b), if evaluated in the time-averaged space, this component gives rise to a sort of four-pole pattern displaying a weak modulation in time (not shown). In previous studies (see, e.g., Ref. 64), one of the remarkable flow features of both Boger and shear-thinning

viscoelastic fluids has been found to be vortex formation and vortex enhancement near corners and other similar geometrical features, which is in line with the present findings.

The most striking effect produced by an increase in Ra_ω can be appreciated in Fig. 15, where for $Gs = 2 \times 10^3$ a significant change in the smoothness of the time-averaged streamlines also starts to develop.

Although the dynamics are basically the same already described for smaller values of the Gershuni number, the shape of the streamlines, previously slightly undulated, exhibits an evident corrugation.
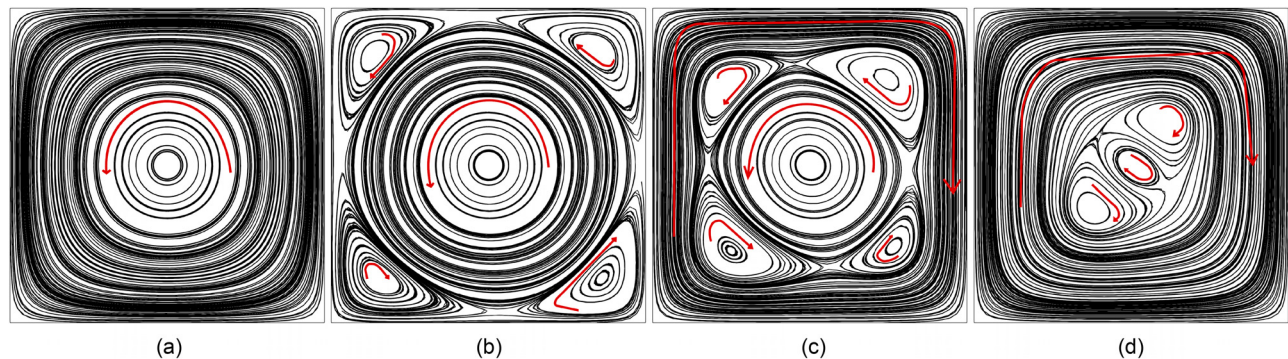

FIG. 11. Streamlines of the total velocity $\mathbf{u}$, $Pr_g = 10$, $Gs = 5 \times 10^2$, $\Omega = 10^2$, $Ra_\omega = 10^3$, $\vartheta = 0.1$, and $\Sigma = 1.6$. Thermovibrational convection in viscoelastic fluid. Details of the inversion of the central cell in the neighborhood of $T_\omega / 4$. (a) $t = 0.3539$, (b) 0.3557, (c) 0.3566, and (d) 0.3575.
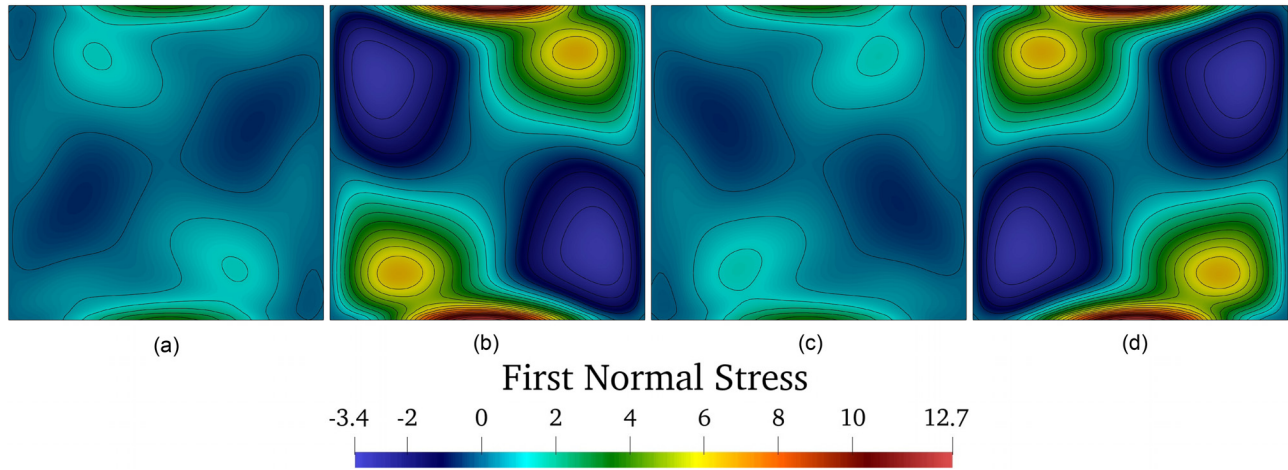
First Normal Stress

-3.4 -2 0 2 4 6 8 10 12.7

FIG. 12. First normal stress, $Pr_g = 10$, $Gs = 5 \times 10^2$, $\Omega = 10^2$, $Ra_\omega = 10^3$, $\vartheta = 0.1$, and $\Sigma = 1.6$. Thermovibrational convection in viscoelastic fluid. Four snapshots equally spaced in time within the oscillation period T_ω. (a) $t_0 = 0.34$, (b) $t = t_0 + T_\omega/4$, (c) $t = t_0 + T_\omega/2$, and (d) $t = t_0 + 3/4T_\omega$.

The center of the main vortex [compare Figs. 10(b) and 15(b)] moves from the middle of the cavity to a position closer to the corner. Figure 15(c) also reveals that the transitional multicellular structure (established in a certain sub-interval of the period T_{umean}) is now distorted and the overall pattern is no longer *symmetric* (as it was in the previous case with respect to the vertical mid-plane). Moreover, the distortions, due to elastic effects, tend to generate smaller cells inside the four bigger central rolls [see Fig. 15(c)].

Quite surprisingly, as a fleeting glimpse into Fig. 16 would confirm, a further increase in the vibrational Rayleigh number ($Ra_\omega = 2.32 \times 10^3$, $Gs = 2.7 \times 10^3$) leads to a mode of convection that is more ordered. A relatively extended central vortex is still produced; however, in this case, its shape resembles an inclined cross with the branches oriented along the diagonals of the cavity. A preferred (main) diagonal, i.e., the south-west to north-east one [see, e.g.,

Figs. 16(a) and 16(b)], can still be identified in certain stages of evolution. A switch in this preferred direction, however, occurs every half period. In the corners not occupied by the central vortex, i.e., the corners lying on the secondary diagonal, three smaller independent eddies (for each corner) appear. Notably, their size increases until they occupy a region that is approximately 1/8 of the total area of the square cavity. During this evolution, a radial distribution of the cells, resembling the aforementioned radial mode of time-averaged convection [depicted in Fig. 8(b) for the Newtonian case], can be recognized. There is indeed a notable analogy between these two modes of convection. Some differences can be identified as well. The outer boundary of the cells is not smooth and displays some undulations. Besides, several smaller secondary eddies, not present in Newtonian liquids, are located in proximity to the walls. A further increase in Ra_ω has the effect to reduce the size of the small rolls located in the corners [Fig.

Shear Stress
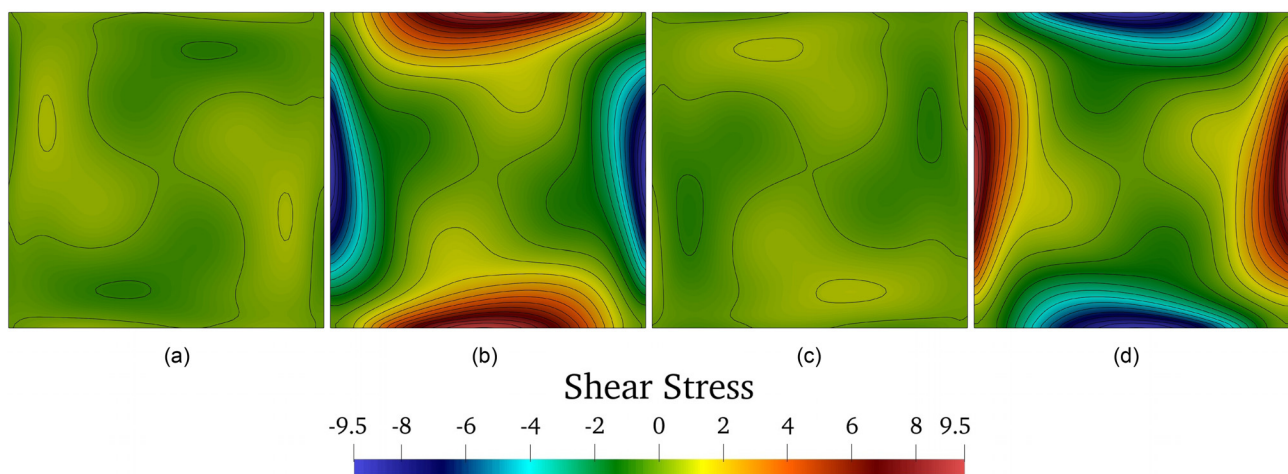
-9.5 -8 -6 -4 -2 0 2 4 6 8 9.5

FIG. 13. Tangential stress, $Pr_g = 10$, $Gs = 5 \times 10^2$, $\Omega = 10^2$, $Ra_\omega = 10^3$, $\vartheta = 0.1$, and $\Sigma = 1.6$. Thermovibrational convection in viscoelastic fluid. Four snapshots equally spaced in time within the oscillation period T_ω. (a) $t_0 = 0.34$, (b) $t = t_0 + T_\omega/4$, (c) $t = t_0 + T_\omega/2$, and (d) $t = t_0 + 3/4T_\omega$.
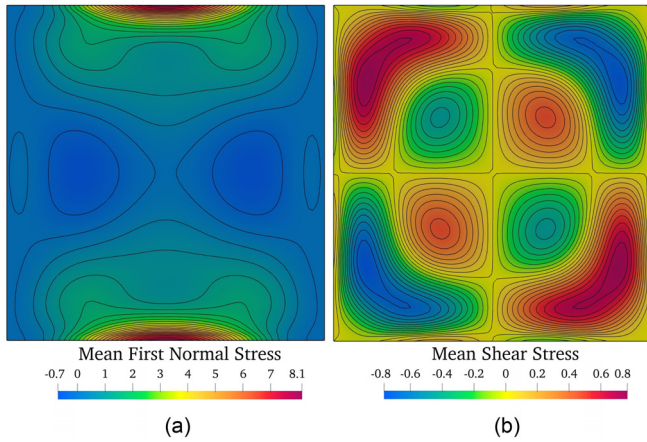
FIG. 14. Mean stress tensor component, $Pr_g = 10$, $Gs = 5 \times 10^2$, $\Omega = 10^2$, $Ra_\omega = 10^3$, $\vartheta = 0.1$, and $\Sigma = 1.6$. Thermovibrational convection in viscoelastic fluid. Snapshot for $t = 39.1$. (a) Mean first normal stress and (b) mean shear stress.

17(b) for the case of $Gs = 3.6 \times 10^3$]. Furthermore, taking a look at the morphological evolution of the main central vortex, it may be concluded that as Gs (Ra_ω) is made higher, the morphology of this cell is gradually transformed from the initially elliptic shape seen in Fig. 15 to a cross-like geometrical configuration [Fig. 17(a)].

Finally, Fig. 18 reports the evolution of the maximum of the instantaneous and time-averaged components of the viscoelastic stress tensor as a function of the Gershuni and the vibrational Rayleigh numbers for fixed ϑ and Ω. Although we did not notice morphological changes in the structure of the patterns already shown in Figs. 12–14 over these ranges of Gs and Ra_ω, the growing behavior of these quantities can clearly be discerned in this figure. This should be seen as a justification for the increasing recognizable importance of the aforementioned "undulations" in the shape of the streamlines. Interestingly, both the fluctuating and the mean components of the viscoelastic stress tensor scale with $Ra_\omega^{1/2}$, which might be seen as a similarity with known behaviors in the Newtonian case for small forcing frequencies such as those considered in the present work (Ref. 65 and references therein).
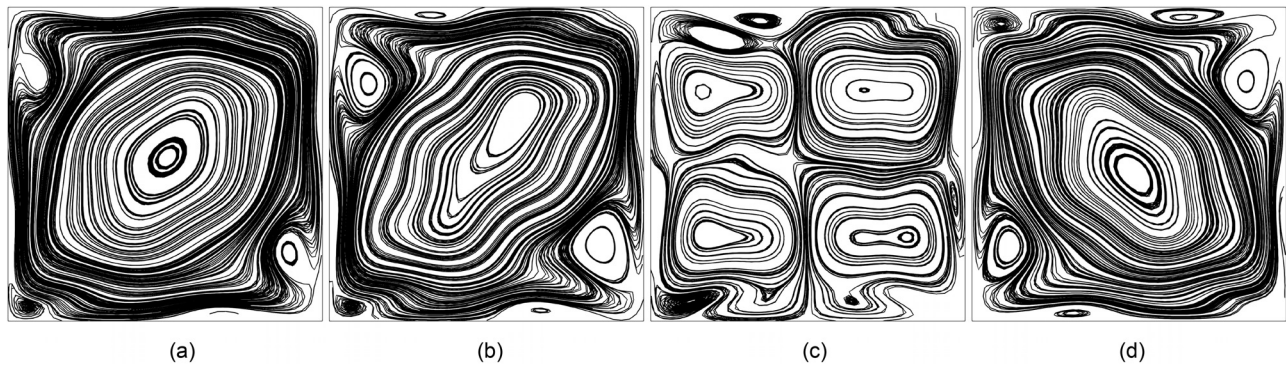

FIG. 15. Streamlines of $\mathbf{u}_{mean}$, $Pr_g = 10$, $Gs = 2 \times 10^3$, $\Omega = 10^2$, $Ra_\omega = 1.61 \times 10^3$, $\vartheta = 0.1$, and $\Sigma = 1.6$. Thermovibrational convection in viscoelastic fluid. Four snapshots equally spaced in time within half oscillation period $T_{umean} \cong 32.1$ (the second part of the period is specular with respect the diagonal of the cavity). (a) $t_0 = 39.2$, (b) $t = t_0 + (1/8) T_{umean}$, (c) $t = t_0 + (1/4) T_{umean}$, and (d) $t = t_0 + (3/8) T_{umean}$.
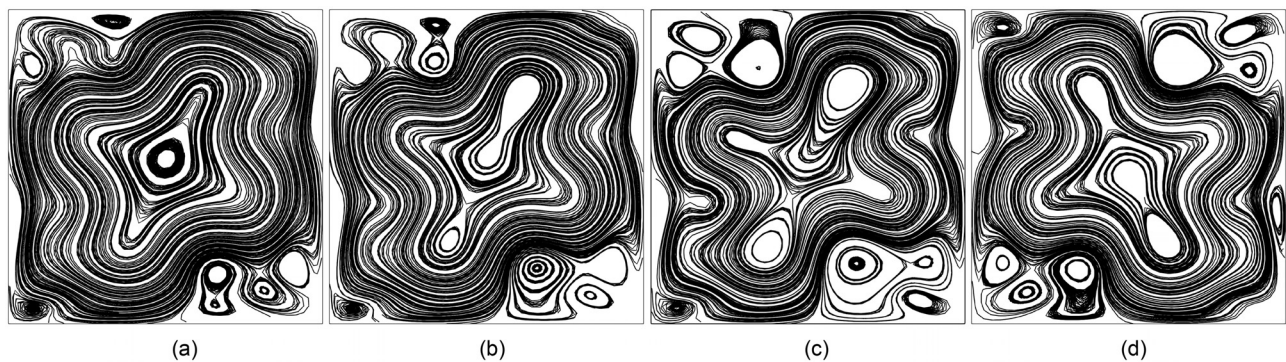

FIG. 16. Streamlines of $\mathbf{u}_{mean}$, $Pr_g = 10$, $Gs = 2.7 \times 10^3$, $\Omega = 10^2$, $Ra_\omega = 2.32 \times 10^3$, $\vartheta = 0.1$, and $\Sigma = 1.6$. Thermovibrational convection in viscoelastic fluid. Four snapshots equally spaced in time within half oscillation period $T_{umean} \cong 33$ (the second part of the period is specular with respect the diagonal of the cavity). (a) $t_0 = 39.15$, (b) $t = t_0 + (1/8) T_{umean}$, (c) $t = t_0 + (1/4) T_{umean}$, and (d) $t = t_0 + (3/8) T_{umean}$.
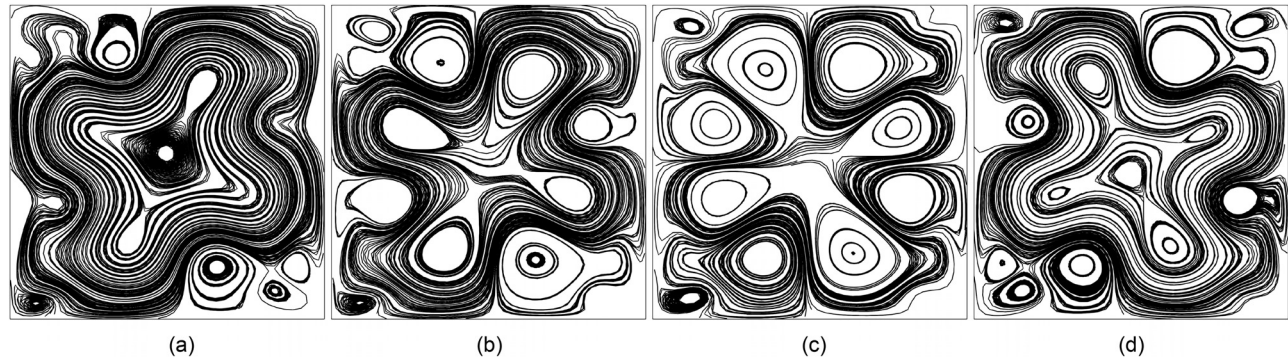
FIG. 17. Streamlines of $\mathbf{u}_{mean}$, $Pr_g = 10$, $Gs = 3.6 \times 10^3$, $\Omega = 10^2$, $Ra_\omega = 2.68 \times 10^3$, $\vartheta = 0.1$, and $\Sigma = 1.6$. Thermovibrational convection in viscoelastic fluid. Four snapshots equally spaced in time within half oscillation period $T_{umean} \cong 33$ (the second part of the period is characterized by dynamics which are specular with respect the diagonal of the cavity). (a) $t_0 = 39.2$, (b) $t = t_0 + (1/8)T_{umean}$, (c) $t = t_0 + (1/4)T_{umean}$, and (d) $t = t_0 + (3/8)T_{umean}$.

Due to viscoelastic singularities, we were prevented from studying situations with $Gs > 3.6 \times 10^3$, this being a well-known problem of this category of liquids (Refs. 45–49).

C. The influence of Σ and ϑ

Having completed a sketch of the situations that can be obtained when Gs is increased for a moderate level of elasticity ($\vartheta = 0.1$ in the preceding section), we now turn to considering the role played in all these dynamics by the triadic interplay existing among the typical characteristic time scales involved in these phenomena, namely, the reference timescale (ℓ^2/α), the fluid relaxation time, and the period of vibrations.

In the non-dimensional space of parameters, these can be reduced to two characteristic numbers only, i.e., ϑ and Σ. As illustrated in Sec. II, these two parameters can be varied independently.

Starting again with the case $\vartheta = 0.1$ ($\Sigma = 1.6$) already shown in Fig. 10, in particular, we have varied the value of the elasticity number in an interval between $\vartheta = 0.2$ and $\vartheta = 0.9$ while keeping fixed Ω. Interestingly, the simulations have revealed that, in a rather unexpected way, higher values of ϑ can produce more ordered phenomena (Fig. 19) with a sequence of stages of evolution that does not change qualitatively as ϑ grows.

The patterning behavior looks really similar to the one already reported in Fig. 8 for a Newtonian fluid. However, a closer look also reveals some differences. Indeed, small eddies are located close to the corners [south-west corner in Fig. 19(a) and north-west/south-east in Fig. 19(d)] and other secondary cells (similar to the ones found for $\vartheta = 0.1$) emerge in proximity to the adiabatic walls [Fig. 19(c)].

A simple rationale for the observed "regularization" of this pattern can be elaborated once again taking into account the influence of the viscoelastic stresses. Along these lines, the curves in Fig. 20 are instrumental in demonstrating that, for a fixed $\Omega = 100$, the instantaneous
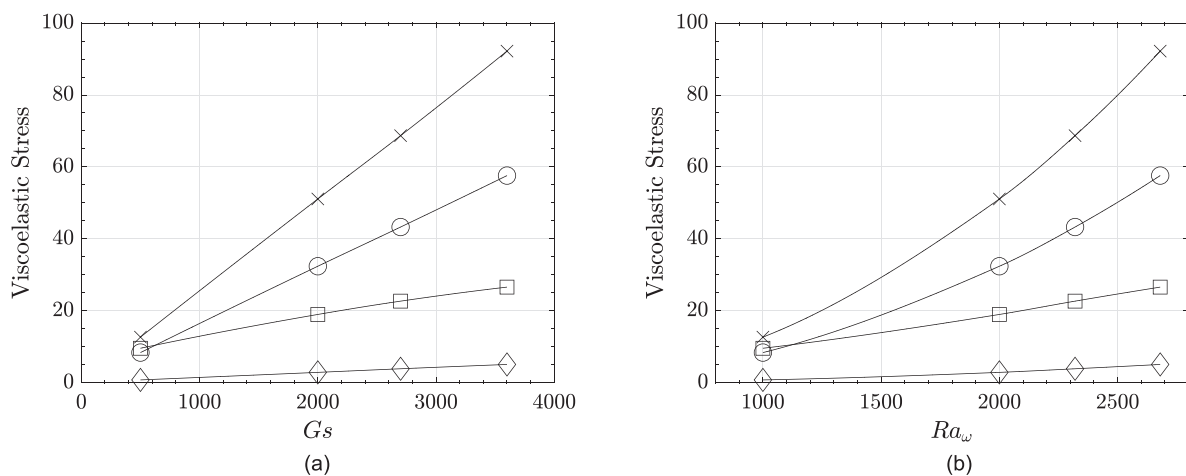

FIG. 18. Representation of the maximum of the instantaneous first normal stress τ_{xx} ($\times$), the time-averaged first normal stress $\tau_{xx,mean}$ ($\circ$), the instantaneous shear stress τ_{xy} ($\square$), and the time-averaged shear stress $\tau_{xy,mean}$ ($\diamond$) as a function of the control parameters. $Pr_g = 10$, $\Omega = 100$, $\vartheta = 0.1$. (a) Variation of the components of $\tilde{\tau}$ and $\tilde{\tau}_{mean}$ as a function of Gs and (b) variation of the components of $\tilde{\tau}$ and $\tilde{\tau}_{mean}$ as a function of Ra_ω.
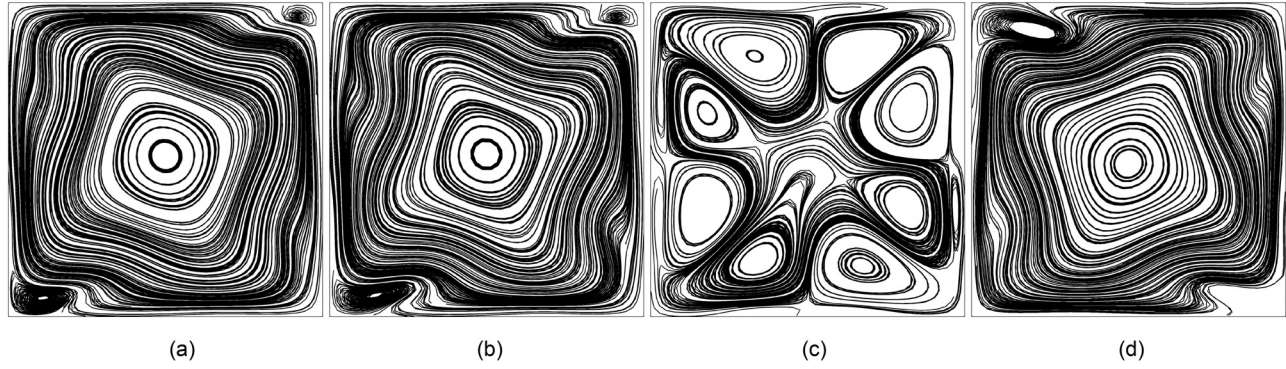
FIG. 19. Streamlines of $\mathbf{u}_{mean}$, $Pr_g = 10$, $Gs = 5 \times 10^2$, $\Omega = 10^2$, $Ra_\omega = 10^3$, $\vartheta = 0.5$, and $\Sigma = 8$. Thermovibrational convection in viscoelastic fluid. Four snapshots equally spaced in time within half oscillation period $T_{umean} \cong 32.1$ (the second part of the period is characterized by dynamics which are specular with respect the diagonal of the cavity). (a) $t_0 = 38.7$, (b) $t = t_0 + (1/8)T_{umean}$, (c) $t = t_0 + (1/4)T_{umean}$, and (d) $t = t_0 + (3/8)T_{umean}$.

and time-averaged components of the viscoelastic stress tensor decrease as a function of ϑ (which varies in the range between 0.1 and 0.9). Although this behavior may look rather counter-intuitive, we wish to recall that similar findings have been reported by other authors for a set of companion problems (Refs. 66–68). In the present case, the related dependencies can be expressed mathematically as follows:

$$\tau_{xx} \approx 0.9\vartheta^{-1.1669}, \tag{21}$$

$$\tau_{xx,mean} \approx 0.354\vartheta^{-1.4429}, \tag{22}$$

$$\tau_{xy} \approx 1.01\vartheta^{-0.9716}, \tag{23}$$

$$\tau_{xy,mean} \approx 0.277\vartheta^{-0.403}. \tag{24}$$

In order to complete the analysis of the different functional dependencies and gain further understanding of the observed dynamics, the sensitivity of the overall fluid-dynamic problem to the Σ parameter has also been assessed. In particular, as shown by Eq. (13), for a fixed ϑ, Σ has been modified by changing Ω.

The case of $\Sigma = 1.6$ has already been analyzed in Sec. IV B. For larger values of this parameter, the simulations show that the pattern comes back to the configuration illustrated in Fig. 2. Interestingly, on increasing Σ, for ϑ fixed to 0.1, the time-averaged viscoelastic tangential stress exhibits a growing trend, whereas its corresponding instantaneous (total) counterpart and the normal stress (both instantaneous and mean versions) become all smaller as Σ grows (Fig. 21). As qualitatively and quantitatively substantiated by Fig. 22, however, an even more interesting scenario can be observed in terms of non-dimensional amplitude and non-dimensional angular frequency of the $\mathbf{u}_{mean}$ signal, measured by a virtual probe located in the center of the cavity.

As evident in this figure, both the curves display a series of maxima and minima. For instance, for $\Sigma = 9.6$ a minimum is attained; the resulting pattern is a quadrupolar distribution of the streamlines with a quasi-stationary behavior. On increasing Σ to 16, the evolution previously shown in Fig. 2 is recovered.
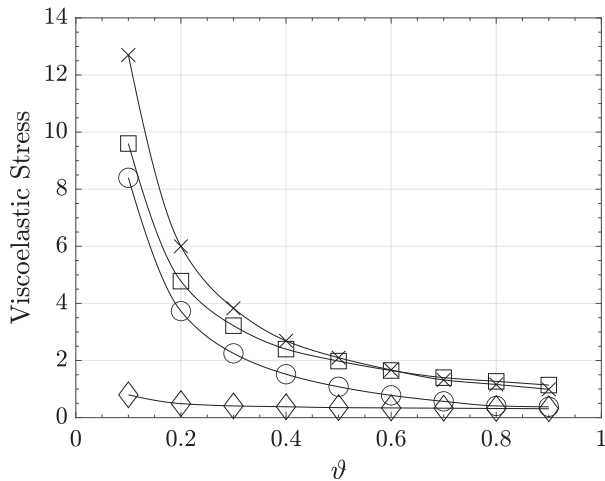

FIG. 20. Variation of the maximum of the instantaneous first normal stress τ_{xx} ($\times$), the time-averaged first normal stress $\tau_{xx,mean}$ ($\circ$), the instantaneous shear stress τ_{xy} ($\square$), and the time-averaged shear stress $\tau_{xy,mean}$ ($\diamond$) as a function of ϑ. $Pr_g = 10$, $\Omega = 100$, $Gs = 5 \times 10^2$, $Ra_\omega = 10^3$.

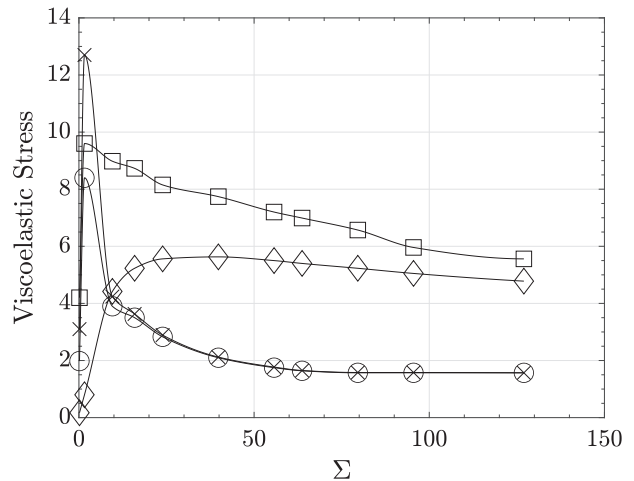**FIG. 21.** Variation of the maximum of the instantaneous first normal stress τ_{xx} ($\times$), the time-averaged first normal stress $\tau_{xx,mean}$ ($\circ$), the instantaneous shear stress τ_{xy} ($\square$), and the time-averaged shear stress $\tau_{xy,mean}$ ($\diamond$) as a function of Σ. $Pr_g = 10$, $Gs = 5 \times 10^2$, $Ra_\omega = 10^3$, $\vartheta = 0.1$, $\Omega \in [10; 8 \times 10^3]$.

This non-monotonic trend obviously calls for a complementary interpretation and, perhaps the most obvious way to do so is to point out that the switching of the trajectory of a system in the space of phases among two or more concurrent attracting sets (as one of the control parameters is changed) is not a new phenomenon in fluid-dynamics, especially when viscoelastic fluids are considered. As illustrated, e.g., by Refs. 18 and 19, convection in viscoelastic fluids is often characterized by the existence of multiple attractors, i.e., solutions which can coexist in the space of phases for a fixed set of input parameters. It is known that the presence of multiple attractors can act as an additional source of apparent randomness in a chaotic system producing sudden and repeated jumps from a branch of solutions to another branch. As an example, a chaotic attractor can reduce to a simple time-periodic flow following a chaos "crisis" similar to that observed in standard Rayleigh-Bénard convection by Paul et al.[69] (this kind of bifurcation can be viewed as a sudden change in the size of the attractor[70]). As also illustrated by Grebogi et al.[71] and Arnold et al.,[72] apparently intermittent behaviors can be induced by the "collision" of a chaotic attractor with an unstable periodic orbit or its stable manifold. Such collisions can drive a system toward a different scenario giving rise to non-monotonic trends similar to that displayed in Fig. 22.

Before being carried away by this fascinating idea, however, one should reflect on the fact that, since in the present case the flow has always been found to be simply periodic, mechanisms based on the crisis of strange attractors, such as those invoked by Ref. 19, should obviously be ruled out.

While a precise clarification of the cause-and-effect relationships underlying such non-monotonic behavior will require tools and methods which are beyond the scope of the present study, here we limit ourselves to pointing out that additional simulations conducted using the Oldroyd-B paradigm have shown no significant departure from the trend summarized in Fig. 22, which indirectly provides evidence that such fascinating dynamics should not be ascribed to the specific viscoelastic model employed (the FENE-CR). Using this observation as a pre-requisite and building on some common principles on which both the Oldroyd-B and the FENE-CR rely, we have elaborated a potentially useful analogy between the present and other known phenomena. The related arguments are based on some notable similarities between two seemingly unrelated branches of physics and engineering (which the interested reader will find in Appendix A).

V. CONCLUSIONS

This research has attempted to assemble a simple, physically intuitive and reasonably self-contained discussion of pure thermovibrational convection in a viscoelastic fluid. A square cavity has been considered given its intrinsic ability to reveal the hidden symmetries of the different convective modes that can be excited in the space of parameters. As made evident by a critical comparison of Newtonian and viscoelastic cases, viscoelasticity can deeply influence the properties of this type of flow.

For Newtonian fluids, the patterning scenario (in terms of time-averaged flow) essentially consists of the alternation of a roll configuration displaying inversional symmetry and a quadrupolar roll distribution. This spatiotemporal behavior is stable over a relatively wide range of values of the Gershuni number. For relatively high values of Gs, the transition to a different pattern occurs gradually and in an ordered way. The shape of the streamlines remains smooth and the

interpretation of the time-dependent flow is relatively straightforward. The number of rolls changes from a minimum of three to a maximum of eight in the range of Gs considered in the present work. Furthermore, specific symmetry properties can be recognized in each case.

For the viscoelastic liquid, the scenario changes dramatically. The regular phenomena displayed by the Newtonian case are taken over by more involved mechanisms, which, for the lowest values of Gs reduce to the alternation between three and twelve principal time-averaged rolls plus four additional small rolls located in proximity to the adiabatic walls. Besides, hand by hand with an increase in the complexity of the pattern, the time-averaged flow displays an increasing sensitivity to Gs (or to Ra_ω for a given value of the forcing frequency). Remarkably, changes are not limited to a qualitative modification of the flow topology. Appreciable variations also affect the magnitude of the time-averaged velocity. As an example, for $Gs = 5 \times 10^2$, $\Omega = 10^2$, and $\vartheta = 0.1$, the amplitude (A) of the signal of time-averaged velocity measured by a probe located in the center of the cavity is $A_{\text{viscoelastic}} = 1.57 \times 10^{-2}$ and $A_{\text{Newt}} = 8.2 \times 10^{-3}$ for the viscoelastic and the corresponding Newtonian fluid, respectively.

The most interesting cases are those where the characteristic time of the vibrations and the relaxation time are comparable. In such conditions, complex dynamics are established due to the competition between the propensity of polymer molecules to return to a relaxed position and the external vibrations that stretch and shrink them on a regular basis. This phenomenon manifests itself with complex patterns characterized by corrugated rolls and with a non-monotonic behavior in the amplitude-Σ plane. The latter trend exhibits a fascinating similarity with the typical behavior of mechanical systems equipped with viscoelastic "components" for vibrational mode control. Notably, viscoelastic flows share a remarkable analogy with these systems in terms of governing equations and physical interpretation of the involved terms (the interested reader being referred to Appendix A).

An exciting prospect for the future is to investigate the corresponding dynamics for the case in which the constraint of two-dimensionality is removed. While for standard (constant gravity) buoyancy convection in the Newtonian case (Refs. 73–76), 3D effects have been shown to be limited to viscosity-induced phenomena in thin regions located in proximity to the sidewalls perpendicular to the spanwise direction, there is no guarantee that a similar concept would be applicable to the viscoelastic case.

APPENDIX A

In this appendix, we consider the evident similarity between the phenomenon reported in Fig. 22 and another category of problems, i.e., that of mechanical systems subjected to vibrations where *viscoelastic* "components" are intentionally used to implement *vibrational mode control*.

Developing this analogy obviously requires understanding how these systems work. In practice, they generally employ a series of viscoelastic parts as connections between sub-structures.[77] From a technical standpoint, such components are used for their renowned ability to provide a good protection against vibrations through generation of deformations (by which a significant part of the available vibrational energy is *dissipated*).
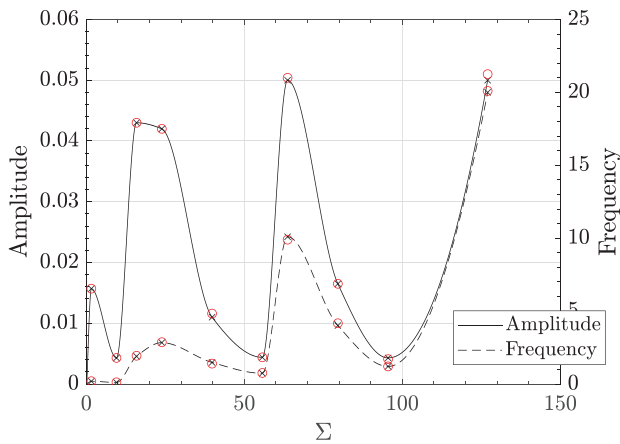
FIG. 22. Variation of the non-dimensional amplitude and the non-dimensional angular frequency of $\mathbf{u}_{mean}$ as a function of Σ. $Pr_g = 10$, $Gs = 5 \times 10^2$, $\vartheta = 0.1$, $\Omega \in [10; 8 \times 10^3]$. The symbols $\times$ and $\circ$ refer to the results obtained with the FENE-CR and the Oldroyd-B, respectively.

In the past, these complex multi-component structures (widely used for disparate applications in engineering) have been characterized in terms of relatively simple models able to provide meaningful information on their behavior in a relatively straightforward way. Such models have generally been built on the basis of rational physical arguments and by turning the original mechanical system into *a network of specialized functions*, each accounting for a specific physical effect.

As an example, since the above-mentioned parts are generally made of materials that have high elasticity and, at the same time, can play the role of energy-dissipating components, each of them can be considered theoretically equivalent to an assembly formed by a spring (with a certain stiffness) and a damper (with a certain energy dissipation coefficient). The simplest case is obviously that of an isolated viscoelastic mass (a single substructure) vibrating under the effect of an external forcing, which can be mimicked or modeled as a simple spring-oscillator model with a single degree of freedom (DOF). If the single spring is assembled with the damper in a side-by-side configuration, the problem can be reduced from a purely mathematical point of view to a single ordinary differential equation $m\ddot{x} + c\dot{x} + kx = f(t, \Omega)$, where m is the mass, c is the damping coefficient, k is the stiffness, and $f(t, \Omega)$ represents the external forcing.

Of course, actual mechanical systems[77] used for vibrational mode control are very complicated and have large amounts of DOFs. For this reason, their mathematical characterization, in general, relies on systems of coupled equations (their number being equal to the number of involved DOFs). These sets of coupled equations have largely been studied over the years due to their ability to predict the so-called "resonances" and "anti-resonances."[77,78] The former simply correspond to the well-known ability of dynamical systems to produce oscillations of relatively high amplitude, not because a particularly chaotic state has been entered, but because the frequency of the forcing has become equal to one (there might be many depending on the number of DOFs) of the frequencies of natural oscillation of the considered system. Vice versa, the latter refers to the remarkable possibility to mitigate the oscillatory behavior induced by an external forcing by taking advantage of the intrinsic elastic response of the system itself. Put simply, this means that

specific frequencies exist for which *a destructive interference* is established between the external driving force and one of the many oscillators present in the considered multi-component structure; most remarkably, it is known that at these frequencies the oscillation amplitude can drop to almost zero.

These resonances and anti-resonances can typically be seen in the so-called amplitude-frequency characteristic curve of the considered system, i.e., a plot reporting the amplitude of oscillation and a function of the frequency of the driving force, where they correspond to peaks and valleys, respectively. These plots (see, e.g., Refs. 77 and 79) are surprisingly similar to that shown in Fig. 22, which may indicate that the dynamics of the vibrated viscoelastic fluid considered in the present work are governed by similar principles. Along these lines and further pursuing the analogy between the present problem and the aforementioned multi-functional structures (consisting of viscoelastic parts subjected to external vibrational forcing), it is worth recalling the fundamental properties of the so-called Dumbbell paradigm on which the viscoelastic models described in Sec. II are based. In the framework of this paradigm, indeed, a viscoelastic fluid can be seen as a combination of a collection of fluid parcels of a solvent (masses) and molecules of polymer (springs).

The analogy set in this way might easily be extended even to the governing mathematics. Although for multi-components mechanical systems it essentially consists of sets of ordinary differential equations, whereas for a viscoelastic fluids the dynamics are governed by partial differential equations, a one-by-one relationship could be established among the related terms: namely, $m\ddot{\mathbf{x}}$, $c\dot{\mathbf{x}}$, $k\mathbf{x}$ and $\mathbf{f}(t, \Omega)$ corresponding to the substantial derivative of the fluid velocity, the Laplacian of velocity (viscous effect), the divergence of the elastic (extra) stress tensor, and the time-dependent buoyancy term in Eq. (9), respectively.

To put our results in a broader perspective and create other useful links with the existing literature, the reader may also consider some other studies appearing recently about the dynamics of viscoelastic fluids in pipe systems. Actually, the idea that the response of viscoelastic fluids to external excitations can provide a new way to control a system with "dynamic modulation functions" is not new and has already been exploited to a certain extent to develop new microfluidic logical components considering the effect of constant or impulsive forces.[80] As another example, most recently, by applying the Oldroyd-B model to the transient response of a viscoelastic Poiseuille flow in a two-dimensional channel for different types of forcing at the inflow, Zhang *et al.*[81] have clearly shown that a state of resonance can be attained if a periodic square wave force is applied and its frequency matches the intrinsic frequency of oscillation of the viscoelastic, i.e., the frequency of the oscillatory flow that would be obtained by applying a force constant in time.

DATA AVAILABILITY

The data that support the findings of this study are available in PURE: https://doi.org/10.15129/dfd6c952-0c12-4588-8efa-5c8892cab20f.

REFERENCES

[1]F. H. Garner and A. H. Nissan, "Rheological properties of high-viscosity solutions of long molecules," Nature **158**, 634–635 (1946).

[2]R. I. Tanner, "A new inelastic theory of extrudate swell," J. Non-Newtonian Fluid Mech. **6**, 289–302 (1980).

[3]D. F. James, "Open channel siphon with viscoelastic fluids," Nature **212**, 754–756 (1966).

[4]A. B. Metzner, "Behavior of suspended matter in rapidly accelerating viscoelastic fluids: The uebler effect," AIChE J. **13**, 316–318 (1967).

[5]A. G. Fredrickson, *Principles and Applications of Rheology* (Prentice-Hall, 1964).

[6]R. J. Gordon and C. Balakrishnan, "Vortex inhibition: A new viscoelastic effect with importance in drag reduction and polymer characterization," J. Appl. Polym. Sci. **16**, 1629–1639 (1972).

[7]S. Rosenblat, "Thermal convection in a viscoelastic liquid," J. Non-Newtonian Fluid Mech. **21**, 201–223 (1986).

[8]H. M. Park and H. S. Lee, "Hopf bifurcations of viscoelastic fluids heated from below," J. Non-Newtonian Fluid Mech. **66**, 1–34 (1996).

[9]H. M. Park and D. H. Ryu, "Hopf bifurcation in thermal convection of viscoelastic fluids within finite domains," J. Non-Newtonian Fluid Mech. **101**, 1–19 (2001).

[10]H. M. Park and D. H. Ryu, "Nonlinear convective stability problems of viscoelastic fluids in finite domains," Rheol. Acta **41**, 427–440 (2002).

[11]H. M. Park and D. H. Ryu, "Rayleigh–bénard convection of viscoelastic fluids in finite domains," J. Non-Newtonian Fluid Mech. **98**, 169–184 (2001).

[12]H. M. Park and J. Y. Lim, "A new numerical algorithm for viscoelastic fluid flows: The grid-by-grid inversion method," J. Non-Newtonian Fluid Mech. **165**, 238–246 (2010).

[13]H. M. Park and K. S. Park, "Rayleigh-bénard convection of viscoelastic fluids in arbitrary finite domains," Int. J. Heat Mass Transfer **47**, 2251–2259 (2004).

[14]H. M. Park, K. S. Shin, and H. S. Sohn, "Numerical simulation of thermal convection of viscoelastic fluids using the grid-by-grid inversion method," Int. J. Heat Mass Transfer **52**, 4851–4861 (2009).

[15]H. M. Park, "Peculiarity in the rayleigh-bénard convection of viscoelastic fluids," Int. J. Therm. Sci. **132**, 34–41 (2018).

[16]Z. Li and R. E. Khayat, "Finite-amplitude rayleigh–bénard convection and pattern selection for viscoelastic fluids," J. Fluid Mech. **529**, 221–251 (2005).

[17]T. Lyubimova, "Convection of non-newtonian liquids in closed cavities heated from below," Fluid Dyn. **9**, 319–322 (1975).

[18]M. Lappa and A. Boaro, "Rayleigh–bénard convection in viscoelastic liquid bridges," J. Fluid Mech. **904**, A2 (2020).

[19]M. Lappa and H. Ferialdi, "Multiple solutions, oscillons, and strange attractors in thermoviscoelastic Marangoni convection," Phys. Fluids **30**, 104104 (2018).

[20]P. Parmentier, G. Lebon, and V. Regnier, "Weakly nonlinear analysis of Bénard–Marangoni instability in viscoelastic fluids," J. Non-Newtonian Fluid Mech. **89**, 63–95 (2000).

[21]K. X. Hu, M. He, and Q. S. Chen, "Instability of thermocapillary liquid layers for Oldroyd-B fluid," Phys. Fluids **28**, 033105 (2016).

[22]W. M. Yang, "Stability of viscoelastic fluids in a modulated gravitational field," Int. J. Heat Mass Transfer **40**, 1401–1410 (1997).

[23]T. Lyubimova and K. Kovalevskaya, "Gravity modulation effect on the onset of thermal buoyancy convection in a horizontal layer of the Oldroyd fluid," Fluid Dyn. Res. **48**, 061419 (2016).

[24]I. B. Simonenko, "A justification of the averaging method for a problem of convection in a field of rapidly oscillating forces and for other parabolic equations," Math. USSR-Sb. **16**, 245–263 (1972).

[25]S. Zen'kovskaya and I. B. Simonenko, "Effect of high frequency vibration on convection initiation," Fluid Dyn. **1**, 35–37 (1966).

[26]R. Savino and M. Lappa, "Assessment of thermovibrational theory: Application to G -jitter on the space station," J. Spacecr. Rockets **40**, 201–210 (2003).

[27]G. Z. Gershuni and A. V. Lyubimov, *Thermal Vibrational Convection*, Vol. 1 (Wiley, England, 1998).

[28]K. Hirata, T. Sasaki, and H. Tanigawa, "Vibrational effects on convection in a square cavity at zero gravity," J. Fluid Mech. **445**, 327–344 (2001).

[29]V. Shevtsova, I. I. Ryzhkov, D. E. Melnikov, Y. Gaponenko, and A. Mialdun, "Experimental and theoretical study of vibration-induced thermal convection in low gravity," J. Fluid Mech. **648**, 53–82 (2010).

[30]A. Mialdun, I. I. Ryzhkov, D. E. Melnikov, and V. Shevtsova, "Experimental evidence of thermal vibrational convection in a nonuniformly heated fluid in a reduced gravity environment," Phys. Rev. Lett. **101**, 084501 (2008).

[31]A. Mialdun, I. I. Ryzhkov, D. E. Melnikov, and V. Shevtsova, "Experimental evidence of thermovibrational convection in reduced gravity," Space Res. Today **171**, 4–6 (2008).

[32]S. Bouarab, F. Mokhtari, S. Kaddeche, D. Henry, V. Botton, and A. Medelfef, "Theoretical and numerical study on high frequency vibrational convection: Influence of the vibration direction on the flow structure," Phys. Fluids **31**, 043605 (2019).

[33]F. Mokhtari, S. Kaddeche, D. Henry, S. Bouarab, A. Medelfef, and V. Botton, "Three-dimensional effect of high frequency vibration on convection in silicon melt," Phys. Rev. Fluids **5**, 123501 (2020).

[34]G. Z. Gershuni and E. M. Zhukhovitskii, "Free thermal convection in a vibrational field under conditions of weightlessness," Sov. Phys. Doklady **24**, 894–896 (1979).

[35]R. Monti, D. Langbein, and, and J. J. Favier, "Influence of residual accelerations on fluid physics and materials science experiments," in *Fluid Sciences and Materials Science in Space: A European Perspective*, edited by H. U. Walter (Springer, Berlin/Heidelberg, 1987), pp. 637–680.

[36]R. Monti, R. Savino, and, and M. Lappa, "Microgravity sensitivity of typical fluid physics experiment," in *The 17th Microgravity Measurements Group Meeting, Cleveland, Ohio, 24–26 March 1998* (1998), Vol. 23, pp. 1–15.

[37]H. Khallouf, G. Z. Gershuni, and A. Mojtabi, "Numerical study of two-dimensional thermovibrational convection in rectangular cavities," Numer. Heat Transfer, Part A **27**, 297–305 (1995).

[38]G. Crewdson and M. Lappa, "The zoo of modes of convection in liquids vibrated along the direction of the temperature gradient," Fluids **6**, 30 (2021).

[39]M. Lappa, "The patterning behaviour and accumulation of spherical particles in a vibrated non-isothermal liquid," Phys. Fluids **26**, 093301 (2014).

[40]M. Lappa, "Numerical study into the morphology and formation mechanisms of threedimensional particle structures in vibrated cylindrical cavities with various heating conditions," Phys. Rev. Fluids **1**, 064203 (2016).

[41]M. Lappa, "On the multiplicity and symmetry of particle attractors in confined non-isothermal fluids subjected to inclined vibrations," Int. J. Multiphase Flow **93**, 71–83 (2017).

[42]M. Lappa, "On the formation and morphology of coherent particulate structures in non-isothermal enclosures subjected to rotating g-jitters," Phys. Fluids **31**, 073303 (2019).

[43]M. Lappa and T. Burel, "Symmetry breaking phenomena in thermovibrationally driven particle accumulation structures," Phys. Fluids **32**, 053314 (2020).

[44]J. Martínez-Mardones and C. Pérez-García, "Bifurcation analysis and amplitude equations for viscoelastic convective fluids," Il Nuovo Cimento D **14**, 961–975 (1992).

[45]A. Bonito, P. Clément, and, and M. Picasso, "Viscoelastic flows with complex free surfaces: Numerical analysis and simulation," in *Numerical Methods for Non-Newtonian Fluids*, Handbook of Numerical Analysis Vol. 16, edited by R. Glowinski and J. Xu (Elsevier, 2011), pp. 305–369.

[46]H. Demir, R. W. Willianms, and F. T. Akyıldız, "The singularities near the corner of a viscoelastic fluid in a 2D cavity," Math. Comput. Appl. **4**, 39–44 (1999).

[47]R. G. Owens and T. N. Phillips, *Computational Rheology* (Imperial College Press, 2002).

[48]M. Renardy, "High weissenberg number asymptotics and corner singularities in viscoelastic flows," in IUTAM Symposium on Non-linear Singularities in Deformation and Flow, edited by D. Durban and J. R. A. Pearson (Springer Netherlands, Dordrecht, 1999), pp. 13–20.

[49]D. Siginer, *Stability of Non-Linear Constitutive Formulations for Viscoelastic Fluids* (SpringerBriefs in Applied Sciences and Technology, 2014).

[50]M. Lappa, "On the nature of fluid-dynamics," in *Understanding the Nature of Science*, Series: Science, Evolution and Creationism, edited by P. L. Editor (Nova Science Publishers Inc., 2019), Chap. 1, pp. 1–64.

[51]R. B. Bird, P. J. Dotson, and N. Johnson, "Polymer solution rheology based on a finitely extensible bead–spring chain model," J. Non-Newtonian Fluid Mech. **7**, 213–235 (1980).

[52]M. D. Chilcott and J. M. Rallison, "Creeping flow of dilute polymer solutions past cylinders and spheres," J. Non-Newtonian Fluid Mech. **29**, 381–432 (1988).

[53]D. L. Brown, R. Cortez, and M. L. Minion, "Accurate projection methods for the incompressible Navier–Stokes equations," J. Comput. Phys. **168**, 464–499 (2001).

[54]N. A. Petersson, "Stability of pressure boundary conditions for stokes and Navier–Stokes equations," J. Comput. Phys. **172**, 40–70 (2001).

[55]S. Armfield and R. Street, "An analysis and comparison of the time accuracy of fractional-step methods for the Navier–Stokes equations on staggered grids," Int. J. Numer. Methods Fluids **38**, 255–282 (2002).

[56]J. L. Guermond, P. Minev, and J. Shen, "An overview of projection methods for incompressible flows," Comput. Methods Appl. Mech. Eng. **195**, 6011–6045 (2006).

[57]C. M. Rhie and W. L. Chow, "Numerical study of the turbulent flow past an airfoil with trailing edge separation," AIAA J. **21**, 1525–1532 (1983).

[58]J. L. Favero, A. R. Secchi, N. S. M. Cardozo, and H. Jasak, "Viscoelastic flow analysis using the software openfoam and differential constitutive equations," J. Non-Newtonian Fluid Mech. **165**, 1625–1636 (2010).

[59]R. Guénette and M. Fortin, "A new mixed finite element method for computing viscoelastic flows," J. Non-Newtonian Fluid Mech. **60**, 27–52 (1995).

[60]J. Martínez-Mardones and C. Pérez-García, "Linear instability in viscoelastic fluid convection," J. Phys. **2**, 1281–1290 (1990).

[61]J. Mizushima, "Onset of the thermal convection in a finite two-dimensional box," J. Phys. Soc. Jpn. **64**, 2420–2432 (1995).

[62]J. Mizushima and T. Adachi, "Sequential transitions of the thermal convection in a square cavity," J. Phys. Soc. Jpn. **66**, 79–90 (1997).

[63]M. Lappa, "Some considerations about the symmetry and evolution of chaotic Rayleigh–Bénard convection: The flywheel mechanism and the "wind" of turbulence," C. R. Méc. **339**, 563–572 (2011).

[64]M. S. N. Oliveira, P. J. Oliveira, F. T. Pinho, and M. A. Alves, "Effect of contraction ratio upon viscoelastic flow in contractions: The axisymmetric case," J. Non-Newtonian Fluid Mech. **147**, 92–108 (2007).

[65]M. Lappa, *Thermal Convection: Patterns, Evolution and Stability*, Vol. 30 (John Wiley & Sons, Ltd., Chichester, England, 2009).

[66]P. J. Oliveira and F. T. Pinho, "Analytical solution for the fully developed channel flow of a phan- thien and tanner fluid," J. Fluid Mech. **387**, 271–280 (1999).

[67]P. J. Oliveira, "An exact solution for tube and slit flow of a FENE-P fluid," Acta Mechanica **158**, 157–167 (2002).

[68]P. J. Oliveira and F. T. Pinho, "Some observations from analytical solutions of viscoelastic fluid motion in straight ducts," in *Proceedings XIIIth International Congress on Rheology* (British Society of Rheology, 2000), Vol. 2, pp. 374–376.

[69]S. Paul, P. Wahi, and M. Verma, "Bifurcations and chaos in large-Prandtl number Rayleigh–Bénard convection," Int. J. Non-Linear Mech. **46**, 772–781 (2011).

[70]M. Kitano, T. Yabuzaki, and T. Ogawa, "Symmetry-recovering crises of chaos in polarization-related optical bistability," Phys. Rev. A **29**, 1288–1296 (1984).

[71]C. Grebogi, E. Ott, and J. A. Yorke, "Crises, sudden changes in chaotic attractors, and transient chaos," Phys. D **7**, 181–200 (1983).

[72]V. I. Arnolf, V. S. Afraimovich, Y. S. Il'yashenko, and L. P. Shil'nikov, *Dynamical Systems v: Bifurcation Theory and Catastrophe Theory* (Springer, Berlin/Heidelberg, 1994).

[73]W. Hiller, S. Koch, and T. Kowalewski, "Three-dimensional structures in laminar natural convection in a cubic enclosure," Exp. Therm. Fluid Sci. **2**, 34–44 (1989).

[74]S. G. Schladow, J. C. Patterson, and R. L. Street, "Transient flow in a side-heated cavity at high Rayleigh number: A numerical study," J. Fluid Mech. **200**, 121–148 (1989).

[75]K. T. A, "Experimental validation of numerical codes in thermally driven flows," in Advances in Computational Heat Transfer, in *Proceedings of the International Symposium* (Begel House, Inc., 1997).

[76]D. E. Melnikov and V. M. Shevtsova, "Liquid particles tracing in three-dimensional Buoyancy-driven flows," Fluid Dyn. Mater. Process. **1**, 189–200 (2005).

[77]D. X. Li, W. Liu, and D. Hao, "Vibration antiresonance design for a spacecraft multifunctional structure," Shock Vib. **2017**, 1–10.

[78]M. P. Asir, A. Jeevarekha, and P. Philominathan, "Multiple vibrational resonance and antiresonance in a coupled anharmonic oscillator under monochromatic excitation," Pramana-J. Phys. **93**, 43 (2019).

[79]Z. Xie, W. Shepard, and K. Woodbury, "Design optimization for vibration reduction of viscoelastic damped structures using genetic algorithms," Shock Vib. **16**, 455–466 (2009).

[80]A. S. R. Duarte, A. I. P. Miranda, and P. J. Oliveira, "Numerical and analytical modeling of unsteady viscoelastic flows: The start-up and pulsating test case problems," J. Non-Newtonian Fluid Mech. **154**, 153–169 (2008).

[81]M. Zhang, W. Zhang, Z. Wu, Y. Shen, H. Wu, J. Cheng, H. Zhang, F. Li, and W. Cai, "Modulation of viscoelastic fluid response to external body force," Sci. Rep. **9**, 9402 (2019).